Università degli Studi di Padova

Dipartimento di Fisica e Astronomia Galileo Galilei

Università degli Studi di Padova

Dipartimento di Fisica e Astronomia "Galileo Galilei"

Corso di Laurea Triennale in Fisica

Tesi di Laurea

Realizzazione di un Setup di Spettroscopia a Correlazione di Fotoni

Realization of a Photon Correlation Spectroscopy Setup

Relatore

Prof. Giulio Monaco
Università degli Studi di Padova

Correlatore

Dr. Jacopo Baglioni
Università degli Studi di Padova

Laureando

Gabriele Ciotti

Anno accademico

2022-2023

Contents

Abstract **3**

Estratto (ITA) **4**

1 Introduction **7**

2 Dynamic Light Scattering theory **8**
2.1 Light Scattering theory in inhomogeneous mediums 8
2.2 DLS and fluctuations 9
2.3 The Homodyne Method 10
2.3.1 Discrete scatter: the Gaussian approximation 11
2.4 Source influence 12
2.5 Particles diffusion and Brownian motion 13

3 Materials and methods: realization of the setup **14**
3.1 General setup configuration 14
3.1.1 The probe branch 14
3.1.2 The cuvette 16
3.1.3 The acquisition branch 17
3.1.4 The camera 19
3.2 Contrast 19
3.3 A priori noise analysis 20
3.3.1 Discrete Correlation Function 21
3.3.2 Environmental noise 21

4 Characterisation measurements **23**
4.1 Collimator and beam expander alignment 23
4.2 Final setup adjustments and camera configuration 24
4.3 The data-sets 25
4.3.1 Data analisys 25
4.3.2 Contrast and intensity distribution 26
4.3.3 Autocorrelation 27

5 Conclusions **31**

Bibliography **32**

Abstract

English version

Photon correlation spectroscopy (also known as dynamic light scattering or quasi-elastic light scattering) is a technique that can be used to study the dynamics of complex fluids or undercooled liquids.

In this Thesis, I have contributed to the construction of a setup for this type of experiments in the Structure of Matter Laboratories of the Padua's DFA, and I have taken part in the first characterisation measurements of this setup. By the end of this work, I have become familiar with an optical setup including a laser and a CCD detector, and with the main characteristics of coherent radiation scattering.

* * *

Italian version

La spettroscopia a correlazione di fotoni (nota anche come diffusione dinamica della luce o diffusione quasi elastica della luce) è una tecnica che può essere usata per sondare la dinamica di fluidi complessi o di liquidi sottoraffreddati.

In questo lavoro di Tesi di Laurea si è contribuito alla realizzazione, nei laboratori di Struttura della Materia del DFA di Padova, di un setup per questo tipo di esperimenti, e si è preso parte alle prime misure di caratterizzazione del setup stesso. Questo lavoro ha permesso di prendere dimestichezza con un setup ottico, che include un laser ed un rivelatore CCD, e con le caratteristiche principali della diffusione di radiazione coerente.

Estratto (ITA)

Durante questo lavoro di Tesi di Laurea è stato realizzato, nei laboratori di *Struttura della materia* del *Dipartimento di Fisica e Astronomia* di Padova, un setup per la *Spettroscopia a correlazione di fotoni (PCS)*. L'esperienza aveva come obiettivo la costruzione e la successiva caratterizzazione del setup stesso attraverso lo studio di campioni di prova: nello specifico, il trasporto diffusivo di micro-sfere di polistirene soggette a moto Browniano fornisce un ottimo sistema-tipo che è possibile descrivere in maniera analitica.

Breve introduzione allo *Scattering Dinamico della Luce (DLS)*

Un mezzo non uniforme, con una costante dielettrica $\varepsilon(\vec{r},t)$ variabile in funzione della posizione e del tempo, quando viene illuminato da radiazione coerente produce un campo di scattering dato dalla sovrapposizione dei singoli contributi provenienti da tutte le aree di coerenza all'interno del campione. Questo campo possiede spesso una struttura granulare, detta a "macchioline" (speckles): dall'analisi di questo pattern è possibile estrarre informazioni sulla dinamica del volume illuminato.

In un esperimento di Diffusione Dinamica (o quasi-elastica) della luce una sorgente di radiazione coerente illumina un campione: il campo scatterato viene dunque misurato tramite un apposito sensore. Se il mezzo presenta delle regioni a diversa ε con una dimensione tipica l, queste genereranno un campo di dipolo ognuna se osservate da una distanza $R \gg \lambda$, dove λ è la lunghezza d'onda della radiazione incidente (da Berne e Pecora [1]); tutta la teoria dello *Scattering Dinamico della Luce* discende da questa osservazione.

È possibile definire la funzione di autocorrelazione omodina dell'intensità luminosa come:

$$g^{(2)}(q,\tau) = \frac{\langle I(q,t)I(q,t+\tau)\rangle}{\langle I(q,t)\rangle^2}$$

dove $I(q,t)$ è l'intensità luminosa misurata sul sensore al tempo t e q è il momento scambiato dai fotoni durante il processo di scattering, le partentesi simboleggiano la media temporale e τ è il cosiddetto "delay". Tramite opportuni calcoli è possibile ricavare che per un sistema soggetto a moto Browniano, risolvendone l'equazione di diffusione associata, vale la seguente relazione:

$$g^{(2)}(q,\tau) = 1 + \exp\left\{-\frac{2t}{\tau_c}\right\} \quad ; \quad \text{dove } \tau_c = (q^2 D)^{-1}$$

dove τ_c è il tempo di coerenza caratteristico dopo il quale il segnale valutato ai tempi t e $t+\tau_c$ è scorrelato, D è il coefficiente di diffusione fornito dalla celeberrima relazione di Stokes-Einstein [2] e q è nuovamente il momento scambiato dai fotoni nell'urto. Questa identità è detta *Relazione di Siegert* [3], e riflette delle importantissime proprietà dell'autocorrelazione di una variabile Gaussianamente distribuita.

Breve descrizione del setup sperimentale

Data l'universalità della Spettroscopia a Correlazione di Fotoni, le varie componenti impiegate nella costruzione del setup sono le medesime per tutti gli esperimenti di Scattering Dinamico della Luce: una sorgente, realizzata attraverso l'utilizzo di un laser infrarosso a $\lambda = 1064.2\,\text{nm}$; un detector, in questo caso una fotocamera infrarossa, ed infine un correlatore, qui sostituito da un software. L'intero apparato può essere così diviso in tre sezioni: un ramo di sonda, la cella contenente il campione ed un secondo ramo di acquisizione.

Il ramo di sonda è necessario al fine generare un fascio di luce coerente per illuminare il campione: è composto da un laser nel vicino infrarosso trasmesso in fibra ottica che viene collimato tramite un apposito collimatore. Il diametro del fascio uscente può essere regolato tramite un *beam expander*: questo sistema è realizzato tramite un semplice telescopio a due lenti, la scelta della cui lunghezza focale permette di cambiare con precisione la dimensione del fascio luminoso. Inoltre, tramite l'utilizzo di un iride (diaframma) posto in corrispondenza del

fuoco delle lenti, è possibile filtrare spazialmente la radiazione incidente. Al fine di mantenere la potenza erogata dal laser stabile, e per rimediare alla scarsa risoluzione dello stesso per valori bassi di intensità luminosa, un assorbitore è posizionato subito prima del campione: dischi con diverso coefficiente di assorbimento possono essere interposti nella direzione del fascio al fine di attenuare l'intensità a valle del ramo.

La cella consisteva di una cuvette in plastica al cui interno sono stati posti i due campioni: il primo consisteva di una sospensione acquosa di micro-sfere di polistirene, mentre nel secondo il solvente era una mistura acqua-glicerolo. Un *power meter* collineare con il fascio incidente e posto dietro la cuvette verificava l'assorbimento della stessa ed ha permesso di allineare correttamente il setup. A 90° rispetto al fascio incidente era posizionato il ramo di acquisizione.

Per questo setup, è stata preferita una configurazione di *imaging*: tramite un'iride ed una lente un'immagine lievemente ingrandita della cella veniva proiettata, dopo essere passata attraverso un opportuno filtro passa-banda, sul CCD. I singoli diffusori non possono essere otticamente risolti; tuttavia modificando l'apertura dell'iride era possibile regolare la dimensione delle speckles che si formavano sul sensore: questa viene infatti determinata dalla risoluzione ottica del ramo. Questo sistema permette di studiare efficacemente aree diverse del campione, dato che una singola speckle è generata dal comportamento collettivo di un singolo sotto-volume ben localizzato.

Dato che, in DLS, il volume illuminato si comporta come una sorgente di segnale casuale, in un singolo pixel del CCD potranno essere presenti un numero di speckles pari a:

$$N = \frac{A}{A_c}$$

dove A è l'area del pixel e A_c è l'area di coerenza sul piano del sensore. Dato che diverse speckles sono indipendenti l'una dall'altra poiché generate da volumi distinti, avere $N > 1$ comporta una diminuzione del contrasto totale. Se invece l'area del sensore è più piccola di quella di una singola speckle, questa sarà sempre coerente con se stessa e dunque non si avrà nessuna perdita di contrasto. In generale la *Relazione di Siegert* deve essere corretta con un termine, detto *grado di coerenza spaziale*, che smorza l'intensità della parte esponenziale.

Nella costruzione del setup sperimentale è necessario tenere conto della presenza di limiti intrinseci alla precisione ottenibile, derivanti o dalla specifica tecnica utilizzata, o dalla natura quantistica della luce (limiti fisici), oppure da contributi ambientali. Per quanto riguarda le limitazioni introdotte dall'apparato, il tempo di acquisizione discreto della camera modifica il calcolo della funzione di autocorrelazione, che ora deve essere corretta come:

$$C^j(k) = \frac{1}{N-k} \sum_{i=1}^{N-k} s_i^j \cdot s_{i+k}^j \quad ; \quad \text{dove } k = \frac{\tau}{\delta t}$$

dove δt è il tempo di acquisizione del sensore, N è il numero totale di frame acquisiti e s_i^j è il segnale registrato dal pixel j-esimo al tempo $t = i \cdot \delta t$. Questa relazione, che prende il nome di *funzione di autocorrelazione discreta*, descrive un approssimazione della vera $g^{(2)}$ e permette di stimare diversi contributi di errore indotti dal processo di discretizzazione.

Infine, la componente di rumore ambientale contribuisce in maniera preponderante all'errore associato alla stime effettuate, ed in particolar modo influisce sul tempo di coerenza. Questa si presenta sotto forma di vari termini quali: fluttuazioni di intensità del laser, presenza di componenti riflesse, impurità all'interno della cella (che generano decadimenti secondari nella funzione di autocorrelazione o fluttuazioni di intensità), polvere sui componenti ottici passivi, vibrazioni meccaniche ed infine rumori termico ed elettronico del sensore. Infine la presenza moti convettivi dovuti al riscaldamento della cuvette indotto dal laser stesso, assieme alla possibile formazione di bolle, può portare ad una decoerenza più rapida a causa del fatto che i singoli volumi di scattering si muovono all'interno del campione.

Breve descrizione della caratterizzazione dell'apparato sperimentale

L'ultima parte di questo lavoro di Tesi di Laurea completa la discussione inerente la calibrazione del setup sperimentale e presenta i risultati della caratterizzazione effettuata. Svolgendo diverse tipologie di analisi, è stato possibile verificare che tutti i componenti del setup si comportassero come previsto.

Come prima cosa è stato verificato, attraverso l'utilizzo di un *beam profiler*, che il fascio proveniente dal ramo di sonda fosse effettivamente collimato. Sono dunque state acquisite diverse misure a varie potenze e distanze dal collimatore per verificarne il corretto allineamento: queste hanno permesso di dimostrare che non è presente asimmetria nelle componenti orizzontali e verticali del profilo del fascio. Successivamente, il laser ed il ramo di acquisizione sono stati allineati, sfruttando il feedback proveniente dalla cuvette stessa. A questo punto l'assorbitore è stato configurato al fine di ottenere l'intensità luminosa desiderata sul campione.

Un totale di 7 data-sets a potenza crescente sono stati acquisiti utilizzando il primo campione: è stato immediatamente possibile osservare come la presenza del rumore abbia fortemente influenzato il segnale proveniente le zone meno illuminate del campione. Per le potenze più alte, inoltre, si è potuto verificare l'instaurarsi di moti convettivi all'interno della cuvette. È di interesse lo studio della distribuzione in potenza del segnale rilevato sul CCD al fine di verificare che l'apparato sia sensibile a fenomeni di scattering con scale diverse di intensità. Teoricamente, il puro speckle pattern dovrebbe presentare una *funzione di densità di probabilità (PDF)* esponenziale (da Goodman [4]); tuttavia la convoluzione con il rumore rende la reale distribuzione una curva piccata con una coda esponenziale. I dati sperimentali acquisiti confermano questa ipotesi. Analizzando inoltre la variazione del contrasto in funzione della posizione sul sensore, è possibile notare la presenza di una zona uniforme centrata in corrispondenza del fascio incidente, compatibile con il campo di speckles osservato, ed un plateau nelle zone non illuminate coerente con la presenza del rumore. Per intensità luminose basse, il contrasto cresce in maniera lineare rispetto alla potenza.

Infine, la teoria dell'autocorrelazione può essere utilizzata per estrarre informazioni riguardanti la distribuzione spaziale delle speckles e la loro decoerenza temporale. Nel *Photon Correlation Imaging* ogni pixel agisce come un detector indipendente, permettendo così di effettuare contemporaneamente misure di DLS su un grande numero di aree di coerenza. Dato che speckles diverse sono scorrelate tra di loro, assumendo che il campione sia spazialmente omogeneo e che la dinamica sia stazionaria, è possibile definire la funzione di autocorrelazione spaziale come:

$$g^{(2)}(\vec{\Delta}) = \left\langle \frac{\langle I(t,\vec{x})I(t,\vec{x}+\vec{\Delta})\rangle_r}{\langle I(t,\vec{x})\rangle_r^2} \right\rangle_T$$

dove $\langle \ldots \rangle_r$ rappresenta la media spaziale su tutto i sensore, $\langle \ldots \rangle_T$ rappresenta la media temporale sui frame acquisiti e $\vec{\Delta}$ è il vettore di "spostamento spaziale". Data l'orientazione del fascio laser rispetto al sensore, è interessante considerare unicamente la dimensione verticale ed orizzontale delle speckles. Dall'analisi di queste funzioni per i diversi set ottenuti con la sospensione acquosa, è stato possibile verificare le considerazioni effettuate. Nonostante globalmente le speckles misurate risultino più grandi delle stime teoriche, il sistema di imaging ha dimostrato di funzionare correttamente.

In ultimo, è stata calcolata l'autocorrelazione temporale in funzione della potenza al fine di estrarre il tempo di decoerenza tipico del sistema in funzione della potenza incidente: fittando i dati ottenuti stavolta da 3 set acquisiti utilizzando il secondo campione, è stato possibile estrarre una stima sperimentale del τ_c. Per potenze più elevate i fenomeni di turbolenza ed il riscaldamento della cuvette hanno portato ad una riduzione del tempo di coerenza.

1

Introduction

The main subject of this experimental Thesis work is the construction, in the *Structure of Matter Laboratories* of the Padua's *Dipartimento di Fisica e Astronomia*, of an optical *Photon Correlation Spectroscopy (PCS)* setup: this technique, also known as dynamic light scattering or quasi-elastic light scattering, can be used to study the dynamics of various materials such as complex fluids, undercooled liquids, foams, gels and glasses. Those materials present heterogeneous temporal dynamics, often with intermittent rearrangements, and are also very heterogeneous in space, behaving very differently in different regions of the sample at equal time.

When a light beam impinges on a medium, the illuminated volume will produce a scattering field generated by the superposition of the individual contributions from each sub-region in the sample. The diffraction pattern often shows a grainy random structure called *speckle pattern*: different individual scattered fields interfere constructively or destructively, leading to a randomly fluctuating far-field scattering figure, the speckle pattern indeed. Information regarding the dynamics of spatially correlated volumes in the medium is encoded in this random pattern.

This Thesis will focus on the construction and the first characterisation measurements of the setup using test samples: the work aims to study the diffusive transport of micro-metric polyester spheres, which is suitable for a calibration process given the widespread knowledge of Brownian diffusion (first analytically described by Einstein [2]). A feature of this setup is the imaging configuration, which allows us to tune the effective size of the speckles with an iris diaphragm: because of this, a more appropriate denomination for the technique used is *Photon Correlation Imaging (PCI)*.

The Thesis is divided into three parts:

1. The first part introduces the basic principles of *Dynamic Light Scattering (DLS)*, in order to comprehend the scientific problem of the Photon Correlation Spectroscopy. The Brownian particles diffusion's model will also be briefly examined.
2. The second part presents the setup configuration, describing the experimental PCS technique and the optical alignment performed, together with the sample preparation.
3. The last part complete the discussion about the setup calibration and presents the experimental results in the light of the background provided in the previous parts.

This Thesis work required the preparation of software (Python) to calculate the correlation function of the measured light intensity. By the end of this work, I have become familiar with an optical setup including a laser and a CCD detector, and with the main characteristics of coherent radiation scattering.

2

Dynamic Light Scattering theory

In this Chapter the general theory of *Dynamic Light Scattering* experiments will be discussed: a speckle pattern is generated from the interaction of light with a small volume of size superior to the range of spatial correlations, provided that this range is much smaller than the total scattering volume V. From the analysis of this scattering pattern is then possible to infer on the sample's structural and dynamical proprieties. In simple cases a classical analytical model can be developed, leading to a precise description of the behaviour of the system: in most systems the main results of the theory differ little (or not at all) from the full quantum predictions. In the specific case of this Thesis work, the analysis of the speckle pattern allows to study on the global arrangement of the particles in the system.

Even if incident beam is monochromatic, the scattered field will presents a complex structure in the frequency domain due to the inelastic scattering: only the elastic component can be satisfactorily described, and it is more relevant for the purpose of this Thesis. Also, inelastic scattering makes up for a negligible fraction of the total scattering, thus will always be considered negligible [5].

2.1 Light Scattering theory in inhomogeneous mediums

A non-uniform scattering medium, with a time-dependent dielectric constant (e.g. due to small particles suspended in a solution, which change their spatial configuration due to Brownian motion), responds linearly (under certain hypothesis [6]) when a weak coherent light pulse is applied. More precisely, if the material is weakly coupled to the light field, it is only necessary to know how the system behaves in the absence of the coupling, in order to analytically describe the way in which the light field responds to time-dependent changes in the medium.

In DLS experiments, a light beam (often polarized) impinges on a sample: the scattered light is then detected by a sensor [Fig. 2.1]. If the medium is homogeneous, with the exception of surface reflections phenomena, no scattering is observed: in fact, the presence of inhomogeneitys with a correlation length $l > \lambda$. in the local dielectric constant of the medium (here assumed to be scalar, for a more complete discussion refer to Berne and Pecora [1]) is necessary to produce a scattering phenomena. The dielectric constant of the medium can therefore be defined as:

$$\varepsilon(r,t) = \varepsilon + \delta\varepsilon(r,t) \tag{2.1}$$

where $\delta\varepsilon(r,t)$ is the variation of the dielectric constant as a function of position and time with respect to the mean value ε. It is now necessary to make two assumptions, without which an analytical theory of the phenomenon cannot be constructed: most of the photons of the incident beam pass undisturbed through the material, so that the incident beam is not significantly distorted by the medium and the probability of multiple scattering is negligible; this last condition is called hypothesis of *single scattering*.

In the ideal case, therefore, the incident electromagnetic field can be considered to behave as a plane wave:

$$\vec{E}_i(r,t) = E_i \cdot \exp\left[i(\vec{k}_i \cdot \vec{r} - \omega_i t)\right] \hat{n}_i \tag{2.2}$$

Defining the angle θ formed between the incident beam and the sample-to-detector direction as the scattering angle, the linear momentum exchanged by the incident photons with the scattering medium in an elastic interaction

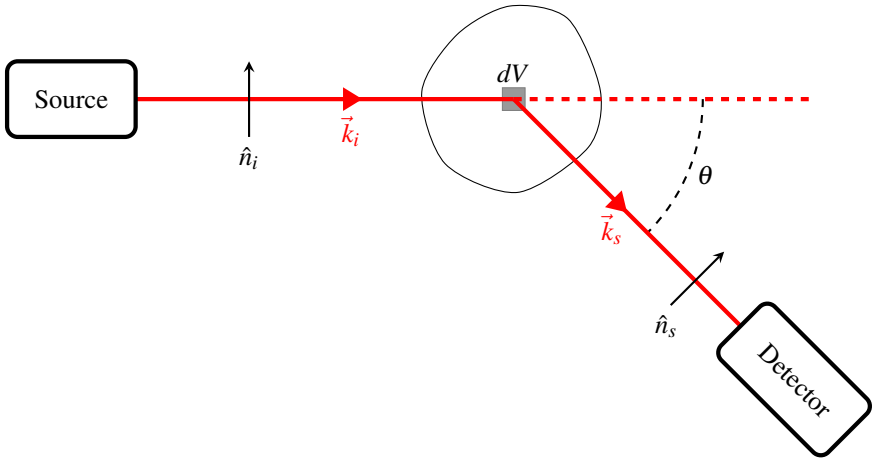

Figure 2.1: *A simplified DLS experimental scheme: a source produces a light beam, which illuminate a sub-region of volume dV. The produced scattered field is then collected by a detector.*

can be calculated as:

$$\vec{q} = \vec{k}_i - \vec{k}_s \quad ; \quad \text{where } q = \frac{4\pi n}{\lambda} \sin\frac{\theta}{2} \tag{2.3}$$

where the wave-vector is orthogonal to the polarisation ($\vec{k}_{i,s} \cdot \hat{n}_{i,s} = 0$), and n is the refractive index of the medium. The intersection between the incident beam, the scattered beam and the medium defines the scattering volume V, i.e. the illuminated area of the sample. The infinitesimal volume giving rise to the scattered photons is called dV. Berne and Pecora showed that the electric field incident on the detector, placed at a large distance ($R \gg \lambda = 2\pi/k_i$) from the sample, is given by [1]:

$$\vec{E}_s(q,t) = -\frac{k_s^2 E_i}{4\pi} \cdot \frac{\exp(\vec{k}_s \cdot \vec{R} - \omega_i t)}{R} \left(\int_V d^3 r \, \frac{\delta\varepsilon(r,t)}{\varepsilon} \exp[-i(\vec{q} \cdot \vec{r})] \cdot \hat{n}_s \right) \tag{2.4}$$

where $d^3 r \equiv dV$. The field is given by the integral extended to the scattering volume of single dipole contributions, where the phase difference is expressed in terms of $\vec{q} \cdot \vec{r}$; also the dipole's strength is modulated by the factor $\delta\varepsilon/\varepsilon$. All light scattering theory descends from [Eq. 2.4], and it is noticeable that the scattering amplitude is codependent from the scattering vector and thus on the local instantaneous variations in the dielectric constant. By analyzing the scattered field pattern, physical information about the sample's behaviour can be extracted.

2.2 DLS and fluctuations

Detectors in light scattering experiments are sensitive to the intensity of the local electric field $I(q,t) \propto |\vec{E}_s(q,t)|^2$, which depends on the exchanged momentum q. Usually in DLS, the time correlation allows to extract information about the sample structure dynamics; for this purpose, the *time autocorrelation function* between two temporal instants (zero and τ) can be defined as:

$$\langle I(q,t) I(q,t+\tau) \rangle = \lim_{T\to\infty} \frac{1}{T} \int_0^T I(q,t) I(q,t+\tau)\, dt \tag{2.5}$$

where, from now on, the angled brackets symbolize the time average. In general $I(q,t) \approx I(q,t+\tau)$ for small values of $\tau \geq 0$, and it is expected that fluctuations in the time correlation function will quickly decouple the intensity value at different times, making the average deviation of $I(q,t+\tau)$ from $I(q,t)$ likely to be non-zero for larger τ values. It follows that:

$$\begin{aligned} \lim_{\tau\to 0} \langle I(q,t) I(q,t+\tau) \rangle &= \langle I(q,t)^2 \rangle \\ \lim_{\tau\to\infty} \langle I(q,t) I(q,t+\tau) \rangle &= \langle I(q,t) \rangle \cdot \langle I(q,t+\tau) \rangle = \langle I(q,t) \rangle^2 \end{aligned} \tag{2.6}$$

Since $I(q,t+\tau) \geq 0$, and in light scattering the fluctuations in the scattered field are random, it results that:

$$\langle I(q,t) I(q,t+\tau) \rangle \leq \langle I(q,t)^2 \rangle \quad ; \quad \forall \tau \geq 0 \tag{2.7}$$

For increasing values of τ the intensity decouples, decaying from a maximum value of $\langle I(q,t)^2\rangle$ to an asymptotic $\langle I(q,t)\rangle^2$, as shown in [Fig. 2.2]. In many applications, such as those mentioned in this Thesis, the correlation function has an exponential decay, and so can be described as:

$$\langle I(q,t)I(q,t+\tau)\rangle = \langle I(q,t)\rangle^2 + \left[\langle I(q,t)^2\rangle - \langle I(q,t)\rangle^2\right]\cdot\exp\left(-\frac{\tau}{\tau_c}\right) \tag{2.8}$$

The relaxation time τ_c is equal to the average fluctuation time of the scattered light, and therefore can provide information about the system decorrelation time. Not all fluctuations' decaying behaviour is exponential: in general, the decay time is defined as the characteristic time at which the autocorrelation function approaches its asymptotic value. A more rigorous definition for the relaxation time is:

$$\tau_c = \int_0^\infty \frac{\langle \delta I(q,t)\delta I(q,t+\tau)\rangle}{\langle \delta I(q,t)^2\rangle} d\tau \tag{2.9}$$

where $\delta I(q,t) = I(q,t) - \langle I(q,t)\rangle$. However, if the autocorrelation function presents non-negligible zero's regions, [Eq. 2.9] does not provide a good estimate of the correlation time. Overall, the relaxation time is a complicated function of the system dynamics, that expresses the decay of the correlations and represents the characteristic time required for $I(q,t)$ and $I(q,t+\tau)$ to get out of phase with each other. In this Thesis work, due to the simplicity of the investigated system, [Eq. 2.9] will always be considered valid.

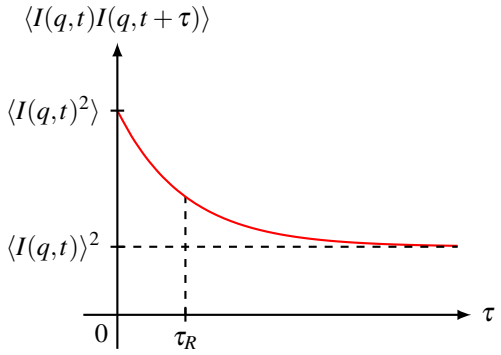

Figure 2.2: *An example of the time autocorrelation function of the scattered intensity in a DLS experiment; τ_c is the characteristic decaying time of the correlation function to the asymptotic value.*

2.3 The Homodyne Method

In the homodyne method, the scattered light from the sample directly impinges on the detector: in a square-law detector, such as the CCD used, the instantaneous output is proportional to the square of the incident electric field and thus to the local light intensity. This means that the sensor can "count" the number of incident photons ($n \propto I(q,t)$) that reach the active area in the exposure time, which in turn is proportional to the dielectric constant fluctuations in the scattering volume, as seen in [Eq. 2.4].

It is useful to define, respectively, the *normalized time correlation functions* of the scattered field and of the light intensity as:

$$\begin{aligned} g^{(1)}(q,\tau) &= \frac{\langle E(q,t)E(q,t+\tau)\rangle}{\langle I(q,t)\rangle} \\ g^{(2)}(q,\tau) &= \frac{\langle I(q,t)I(q,t+\tau)\rangle}{\langle I(q,t)\rangle^2} \end{aligned} \tag{2.10}$$

The $g^{(2)}$ is often referred to as the *normalized homodine correlation function*. If we now consider a system with a scattering volume V, divided into sub-regions of volume dV, the total scattered field is given the superposition of the scattered field from each region, as seen in [Eq. 2.4]. If these regions are large, so that the fluctuations within each of them can be considered independent of the others, then the total field is a sum of independent variables: the central limit theorem implies that $\vec{E}_s$ is a zero mean random variable, and thus Gaussian distributed. In this particular configuration the second moment can characterize the whole distribution, and it is possible to show that [1]:

$$g^{(2)}(q,\tau) = \left|g^{(1)}(q,0)\right|^2 + \left|g^{(1)}(q,\tau)\right|^2 \tag{2.11}$$

where $g^{(1)}$ and $g^{(2)}$ are related to the second and the fourth moments of the Gaussian, respectively. There are situations where this approximation is invalid, for example systems with a long correlation length: in general, the scattering volume must be composed of a sufficiently large number of correlation volumes to justify the use of the theorem. In the case of dilute solutions, such as those studied in this Thesis, the condition translates into having a sufficient concentration of scattering centers.

2.3.1 Discrete scatter: the Gaussian approximation

In this Section, the approximation made in the previous one to calculate the $g^{(2)}$ will be extended to the discrete particles case. In a classical view, the electric dipole moment induced by an external electric field on a spherical particle is given by [7]:

$$\vec{\mu}_E = \hat{\alpha} \cdot \vec{E} \tag{2.12}$$

where $\hat{\alpha}$ is the polarizability tensor in a given set of coordinates. In the case of spherical particles, such as those studied in this Thesis, $\hat{\alpha} = \alpha \cdot \hat{\mathbb{1}}$. If these particles are suspended in a liquid, the local dielectric constant can be written as a function of the position $\vec{R}_i$ of the center of mass of each of the the N-particles in the total volume V (remembering [Eq. 2.1]):

$$\delta\varepsilon(r,t) = \begin{cases} \varepsilon_p(r,t) - \varepsilon & ; \quad \text{if } \vec{R} \in V_i \text{ for at least one } i = 1,\dots,N \\ \varepsilon_l(r,t) - \varepsilon & ; \quad \text{elsewhere} \end{cases} \tag{2.13}$$

where ε is the total average dielectric constant of the individual i-particle; the letters 'p' and 'l' denote, respectively, the particles and the liquid in which they are suspended. Due to the presence of a constant density term $\varepsilon_l - \varepsilon$, which doesn't contribute to the total scattering, it is possible to write:

$$\delta\varepsilon^\star(r,t) = \begin{cases} \varepsilon_p(r,t) - \varepsilon_l & ; \quad \text{if } \vec{r} \in V_i \text{ for at least one } i = 1,\dots,N \\ \varepsilon_l(r,t) - \varepsilon_l = \delta\varepsilon_l(r,t) & ; \quad \text{elsewhere} \end{cases} \tag{2.14}$$

where now the $\delta\varepsilon^\star(r,t)$ is the effective dielectric constant deviation. The scattering volume can be properly divided into M-scattering subregions ($M > N$), so that the first N-regions are centered on the particles center of mass $\vec{R}_i$, and the other $(M-N)$ are all in the suspension medium (this condition is equivalent to $V_{r,j} \cap V_i = \emptyset$; $\forall i = 1,\dots,N \,\&\, \forall j = M-N+1,\dots,M$, where $V_{r,j}$ is the volume of the j-region). If the particles' dielectric constant is significantly different from the average one of the liquid $\varepsilon_p(r,t) \gg \varepsilon_l$, the scattering contribution from the liquid dynamics can be neglected. Of the M sub-volumes only the first N are optically active, meanwhile the spontaneous liquid density fluctuation (at thermal equilibrium) $\varepsilon_l(r,t) \sim \varepsilon_l$ is treated as a constant component and ignored. These contributions could always be separately measured and subtracted from the scattering pattern. it is now possible to define the *single-particle scattering length* of the i-particle as:

$$b_i(q,t) = \frac{k_s^2}{4\pi} \int_{V_i} \frac{\delta_i^\star \varepsilon(r,t)}{\varepsilon} \exp\left[-i(\vec{q}\cdot\vec{r})\right] d^3r \tag{2.15}$$

that matches with the scattering length of the i-th subvolume due to the factor $\delta\varepsilon_i^\star(r,t) = 0$ if $\vec{r} \in V_{r,i} - V_i$; $i = 1,\dots,N$, where N is the number of "active" regions, and thus of particles in the solution. Since the $b_i(q,t)$ are assumed to behave as random variables (the particles in the solution are assumed isolated and not to interact with each other, and so their positions are assumed to be statistically independent), the scattering length becomes constant: for spherical particles, which are isomorphic for rotation, it has the same value for each particle. Using the [Eq. 2.4] and integrating over the volume V, and thus over the N active sub-regions, the total electric field at the sensor position can be obtained:

$$E_s(q,t) = -\frac{E_i \cdot \exp\left(\vec{k}_s \cdot \vec{R} - \omega_i t\right)}{R} b(q,t) \cdot \left(\sum_{i=1}^{N} \exp\left[-i(\vec{q}\cdot\vec{R}_i)\right] \right) \tag{2.16}$$

where $\vec{R}_i$ is the i-th particle position. Because the motion is Brownian, the position of each particle changes randomly as a function of the time such as:

$$\langle \exp\left[-i(\vec{q}\cdot\vec{R}_i)\right] \rangle = \frac{1}{V} \int_V \exp\left[i(\vec{q}\cdot\vec{R}_i)\right] d^3r = \delta(q) \to 0 \quad ; \quad \forall i = 1,\dots,N \quad \Rightarrow \quad \langle E_s(q,t) \rangle = 0 \tag{2.17}$$

where the uniform distribution of the particle positions translates into a probability density $\rho(q) = d^3r/V$ in the ensemble average. As expected, this consideration leads to the average null value of the scattered electric field in [Sec. 2.3], whose module follows a Gaussian distribution. To estimate both the $g^{(1)}$ and the $g^{(2)}$, the mean square module for the scattered electric field, [Eq. 2.16] can be considered; working only on the sum, it is possible

to show that:

$$\left\langle \left| \sum_{i=1}^{N} \exp\left[-i(\vec{q}\cdot\vec{R}_i)\right] \right|^2 \right\rangle = \left\langle \sum_{i,j=1}^{N} \exp\left\{-i\left[\vec{q}\cdot(\vec{R}_i-\vec{R}_j)\right]\right\} \right\rangle = \\ = \sum_{i=1}^{N} 1 + \underbrace{\left\langle \sum_{\substack{i,j=1 \\ i\neq j}}^{N} \exp\left\{-i\left[\vec{q}\cdot(\vec{R}_i-\vec{R}_j)\right]\right\} \right\rangle}_{\to 0} = N \tag{2.18}$$

where the second term, on average, is zero thanks to [Eq. 2.17]. These results are compatible with the random-walk with a zero mean displacement and a mean squared displacement proportional to the number of steps. From [Eq. 2.10], it is possible to express the $g^{(1)}$ as:

$$g^{(1)}(q,\tau) = \frac{1}{N}\left\langle \sum_{i=1}^{N} \exp\left\{-i\vec{q}\cdot\left[\vec{R}_i(0)-\vec{R}_i(\tau)\right]\right\} \right\rangle = \exp\left\{-i\left[\vec{q}\cdot(\vec{R}(0)-\vec{R}(\tau)\right]\right\} \tag{2.19}$$

The homodyne autocorrelation functions can be written instead as:

$$g^{(2)}(q,\tau) = \frac{1}{N^2}\left\langle \sum_{i,j,k,l=1}^{N} \exp\left\{-i\vec{q}\cdot\left[\vec{R}_i(0)-\vec{R}_j(\tau)+\vec{R}_k(0)-\vec{R}_l(\tau)\right]\right\} \right\rangle \tag{2.20}$$

The autocorrelation length is simplified due to the time independence $b(q,t) = b(q,t+\tau)\,\forall\tau \geq 0$. It is possible to separate the contributions where $i=k$, $j=l$ and those coming from $i=l$, $j=k$ with $i\neq j$; all the other terms are zero thanks to [Eq. 2.16] (see [1, 8]). The $g^{(2)}$ can so be expressed as:

$$N^2\cdot g^{(2)}(q,\tau) = \sum_{\substack{i=1 \\ i=j=k=l}}^{N} 1 + \left\langle \sum_{\substack{i,j=1 \\ i=k;\, j=l}}^{N} \exp\left\{-i\vec{q}\cdot\left[(\vec{R}_i(0)-\vec{R}_k(0))+(\vec{R}_j(\tau)-\vec{R}_l(\tau))\right]\right\} \right\rangle + \dots \\ \dots + \left\langle \sum_{\substack{i,j=1 \\ i=l;\, j=k;\, i\neq j}}^{N} \exp\left\{-i\vec{q}\cdot\left[(\vec{R}_i(0)-\vec{R}_i(\tau))-(\vec{R}_j(0)-\vec{R}_j(\tau))\right]\right\} \right\rangle = \\ = N + \sum_{i=1}^{N}\sum_{j=1}^{N} 1 + \left\langle \sum_{\substack{i=1 \\ i\neq j}}^{N} \left(\exp\left\{-i\vec{q}\cdot\left[\Delta\vec{R}_i(\tau)\right]\right\} \cdot \sum_{j=1}^{N} \exp\left\{+i\vec{q}\cdot\left[\Delta\vec{R}_j(\tau)\right]\right\} \right) \right\rangle = \\ = N + N^2 + N(N-1)\left|g^{(1)}(q,\tau)\right|^2 \tag{2.21}$$

where $\Delta\vec{R}_i(\tau) = \vec{R}_i(0) - \vec{R}_i(\tau)$ and, as in [Eq. 2.18], it is possible to separate the particles' dynamics because it was assumed that the behaviour of each one is independent from the others. Taking now the limit for an infinite number of particles (compatible with the Gaussian approximation), it is possible to obtain:

$$\lim_{N\to\infty} g^{(2)}(q,\tau) = 1 + \left|g^{(1)}(q,\tau)\right|^2 \tag{2.22}$$

the same result found in [Eq. 2.11] if it is taken into account that $g^{(1)}(q,0) = 1$. This equation is called the *Siegert relation* [3], and reflects important properties of the correlation functions of a Gaussian variable.

2.4 Source influence

If the scattering volume has a dimension $\sqrt[3]{V} < l_{coh}^{source}$, each point feeds on the same incident electric field. Using [Eq. 2.16], it is possible to separate the scattered field in a component from the incident field, and another given by the scattering dynamics $E_s(q,t) = E_0(q,t)\cdot B(q,t)$, where:

$$B(q,t) = \sum_{i=1}^{N} b_i(q,t)\cdot\exp\left[-i(\vec{q}\cdot\vec{R}_i)\right] \tag{2.23}$$

$B(q,t)$ is called *total scattering amplitude*, referring to the *single-particle scattering length* $b_i(q,t)$ defined in [Eq. 2.15]. The two contributes are independent random variables, and so they can be separated in the time average:

$$\langle I(q,t)\rangle = \langle E_s(q,t)\cdot E_s^{\star}(q,t)\rangle = \langle E_0(q,t)\cdot E_0^{\star}(q,t)\rangle \cdot \langle B(q,t)\cdot B^{\star}(q,t)\rangle \tag{2.24}$$

The normalized autocorrelation function, using the definition of $g^{(2)}$ from [Eq. 2.10], factorize in:

$$g^{(2)}(q,\tau) = g^{(2)}_{source}(q,\tau)\cdot g^{(2)}_{scatter}(q,\tau) \xrightarrow{\tau \gg \tau_{source}} g^{(2)}_{scatter}(q,\tau) \tag{2.25}$$

where, if the system presents a slower dynamics than the source, $g^{(2)}_{source}(q,\tau)\to 1$ [Eq. 2.6, 2.22]: the faster coherence time allows to approximate $g^{(2)}_{scatter}(q,\tau+\tau_{source}) \approx g^{(2)}_{scatter}(q,\tau)$.

2.5 Particles diffusion and Brownian motion

This Section illustrates the relationship between the Brownian motion of spherical particles and the scattering pattern obtained via PCS. The displacement of a particle is represented by a random variable with a Gaussian probability distribution (this follows from the central limit theorem):

$$p\left(\Delta\vec{R}(t)\right) = \left[\frac{3}{2\pi\langle\Delta R^2(t)\rangle}\right]^{3/2}\cdot\exp\left\{\frac{-3\left(\Delta\vec{R}(t)\right)^2}{2\langle\Delta R^2(t)\rangle}\right\} \tag{2.26}$$

where $\Delta\vec{R}(t) = \vec{R}(0) - \vec{R}(t)$ is defined as above. From the diffusion theory, the classical equation that a particle has to satisfy is expressed as:

$$\frac{\partial}{\partial t}p\left(\Delta\vec{R}(t)\right) = D\cdot\nabla^2 p\left(\Delta\vec{R}(t)\right) \tag{2.27}$$

where D is the *diffusion coefficient*, and the nabla expresses the spatial derivative. The Fourier transform of the probability density of the displacement has a form:

$$\tilde{p}\left(\Delta\vec{q}(t)\right) = \exp\left\{-\frac{\Delta q^2\langle\Delta R^2(t)\rangle}{6}\right\} \tag{2.28}$$

and, for a free particle, $\langle\Delta R^2(t)\rangle = \langle v^2\rangle t^2$ with v the velocity of the particle. Substitution in 2.28 leads to (for the full demonstration, see [1]):

$$\langle\Delta R^2(t)\rangle = 6Dt \tag{2.29}$$

The free-particle diffusion constant is given by the celebrated Stokes-Einstein equation [2]:

$$D = \frac{k_B T}{\gamma} \tag{2.30}$$

where k_B is the Boltzmann constant, T is the temperature and γ the drag coefficient, which for spheres is given by $\gamma = 6\pi\eta a$, where η is the shear viscosity of the suspension medium (considered at a fixed temperature) and a is the particles radius. This relation is valid only for slow free-moving particles (scattering between the particles is assumed to be negligible) in a long observation period.

Substituting [Eq. 2.29] into [Eq. 2.19], it is possible to extract the normalized autocorrelation function:

$$g^{(1)}(q,t) = \exp\left\{-q^2Dt\right\} = \exp\left\{-t/\tau_c\right\} \qquad ; \qquad \text{where } \tau_c := (q^2D)^{-1} \tag{2.31}$$

the exponential decay is similar to the example in [Sec. 2.2] and [Fig. 2.2]. Since the relaxation time τ_c is related to the particles size, it is possible to derive the radius a from experimental measurements. The homodyne correlation function takes the form, from [Eq. 2.22]:

$$g^{(2)}(q,t) = 1 + \exp\left\{-2q^2Dt\right\} = 1 + \exp\left\{-2t/\tau_c\right\} \tag{2.32}$$

3

Materials and methods: realization of the setup

The experimental setup has been originally designed to investigate light-induced structural relaxation of non transparent inorganic glass belonging to the vast family of chalcogenide glasses (ChGs): a light source with suitable frequency can stimulate those excitation, thanks to low energy band gaps present in the glasses themselves [9].

Due to the fact that those materials are opaque in the visible spectrum, but presents a transmission maximum in the near infrared, a 1064 nm near-IR laser was used to probe the samples. A multi-pixel acquisition device is also required in PCS: a CCD camera provides a way to perform multiple Dynamic Light scattering measurements at the same time on a large number of speckles.

This Chapter examines the construction of the entire setup, with particular attention to the choice of components used and the issues encountered during the assembly, alignment and calibration of the setup itself. Due to the specific analysis requested, it was essential to exclude or overlook various noise components, thereby influencing the choice of components themselves.

3.1 General setup configuration

Due to the universality of DLS, the main components employed in any light scattering setup (as presented in [Sec. 2.1]) are the same: a light source, realized through the use of a laser; the detector, in this case an infrared CCD; and a signal analyser, which is substituted by a correlation software. The camera branch was designed to operate in an imaging configuration: this allowed to take advantage of both the better statistics given by multi-speckles data, and to obtain a spatially-resolved image of the sample, in order to verify that the dynamics is uniform throughout all the scattering medium (see [Sec. 3.3.2]).

The components were placed in an optical cage system, rather than the more common "floating" configuration, in order to ensure a greater precision and stable alignment along the beam axis (hereafter referred to as the z-axis in the chosen reference system). A scheme of the setup is shown at [Fig. 3.1].

3.1.1 The probe branch

In order to avoid the first term of [Eq. 2.25], a coherent focused source is required to probe the sample. A diode-pumped *Cobolt 05-01 Rumba* laser was used to achieve a suitable correlation length: it has a nominal maximum output power of 500 mW and an operating wavelength of (1064.2 ± 0.6) nm at $25\,^{\circ}C$ (from *Hübner Photonics* [10]). The coherence length of the laser can be calculated as:

$$\tau_{laser}^{coh} = \frac{1}{\Delta\nu} > 1\,\mu\text{s} \quad \Rightarrow \quad l_{laser}^{coh} = c \cdot \tau_{laser}^{coh} \gtrsim 300\,\text{m} \tag{3.1}$$

where $\Delta\nu < 1$ MHz is the dispersion in the frequency domain. It has to be noted that the setup itself has a total optical length < 1 m, which is insufficient for the beam to lose the temporal coherence. The laser guarantees the required propriety, as well as intensity stability (fundamental for DLS).

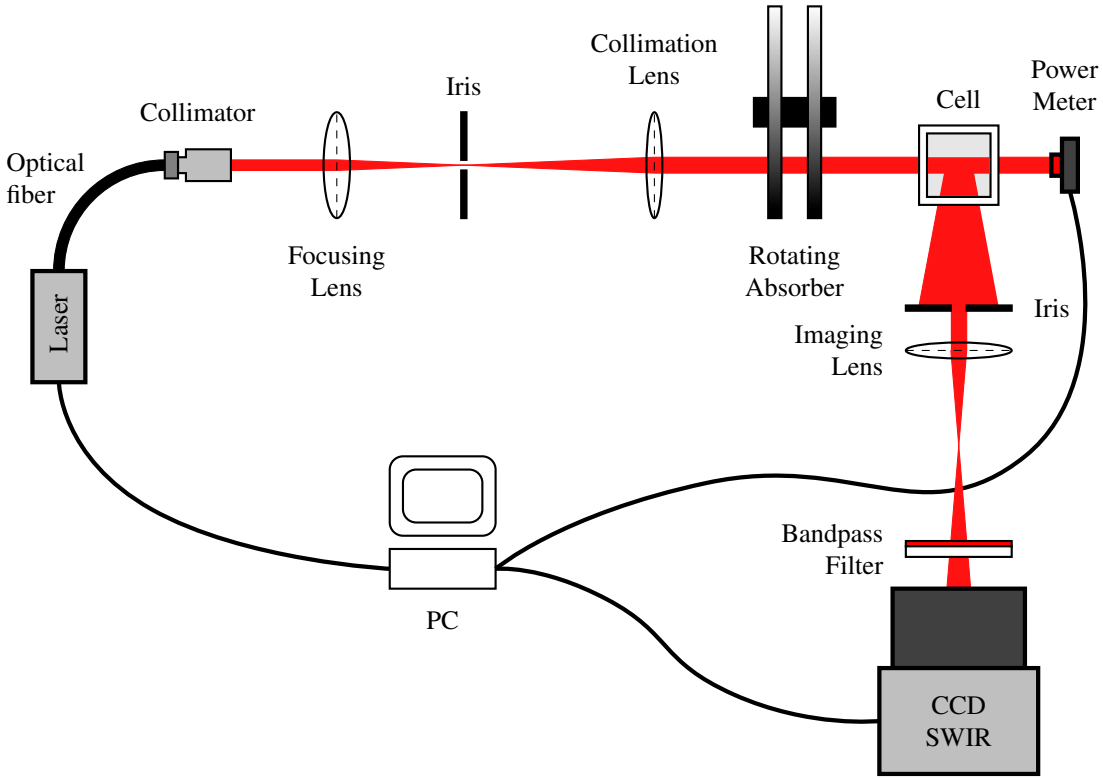

Figure 3.1: *Scheme of the experimental setup (not to scale). The laser probe is sent via optical fibre to a collimator, the beam is then expanded by a simple telescope system and its intensity is regulated by an absorber. A power meter was used to verify the power stability of the laser. The light scattered from the cell is then collected at an angle of 90° from the direction of the incident beam by the camera branch, which consists of an imaging system and a bandpass filter; finally, the signal is collected by the CCD.*

The laser has a beam aperture of $2r = (1000 \pm 50)\,\mu$m at 4σ and was transmitted through an optical fibre to a collimator, which required an alignment to focus and shape the beam: it was important that the cross-section of the beam was circular, because in a non-symmetric geometry the asymmetry of the intensity profile could lead to significant differences in the scattering profile from an inhomogeneous medium. This discrepancy becomes relevant when the presence of a pump laser is taken into account: in the final configuration of the setup, another laser will be used to induce light-induced relaxations in glasses; it is therefore necessary to focus the probe in order to explore only a quasi-constant intensity area of the pump illuminated section. If this condition is not satisfied, the probe laser could illuminate regions with different dynamics, making impossible to separate the signal which instead comes from the "active" zone.

To adjust the beam diameter, a beam expander was introduced: it consisted of a small telescope [Fig. 3.2], with a simple two-lens system used to unfocus the beam and eliminate eventual reflexes. To vary the beam diameter, the two lenses had a different focal lengths $f_{1,2}$, where the magnification is given by:

$$G = \frac{r'}{r} = \frac{f_2}{f_1} \tag{3.2}$$

The iris diaphragm, placed in correspondence of the common focal points of both the focusing and the collimation lenses, has (supposedly) removed any remaining noise components from the beam. Acting as a low-pass filter, the optimal theoretical aperture for the diaphragm can be estimated provided that the resolving power of the system is equal to the beam size. A circular laser beam focused by a lens forms an Airy disc pattern at the focus; the size of this disc is determined by the Abbe criteria:

$$r = J_1 \frac{\lambda}{NA} \quad \Rightarrow \quad s^{th} = 2J_1 \frac{\lambda \cdot f_1}{r} \simeq 1.6\,\text{mm} \tag{3.3}$$

where $J_1 \sim 1.22$ is the first kind Bessel function of order one width, the *Numerical Aperture* is defined by $NA \approx n \cdot s/(2f_1)$, s is the iris diameter and $n \simeq 1$ is the refractive index. This relation is symmetric, considering that [Eq. 3.2] states that $r \cdot f_2 = r' \cdot f_1$. The lens chosen for the setup have a focal lengths of $f_1 = 30\,$cm and $f_2 = 60\,$cm, for a total magnification of $G = 2$.

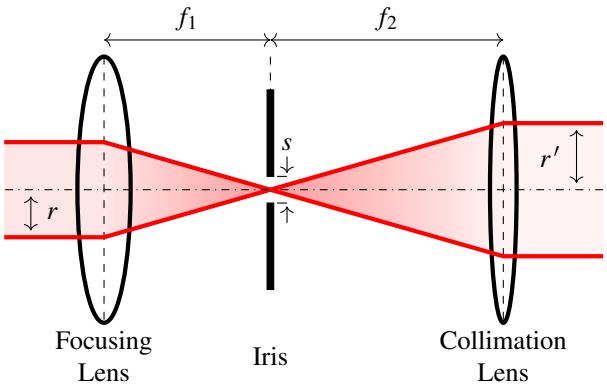

Figure 3.2: *Scheme of the beam expander of the setup (not to scale).*

This consideration only applies to uniform beams: a Gaussian beam will be clipped because some power is blocked at the edge of the diffraction disc, which also increases its divergence; spherical aberration also limits the resolution by broadening the Airy disc at the lens focus. Any eventual distortion in the beam profile would have been magnified by the telescope: it was essential to ensure that the incident beam was symmetrical.

To optimize the stability of the beam, the laser was kept at a fixed operating power for the majority of measurements; to compensate for the power resolution of the laser, it was necessary to introduce an absorber: with absorbing discs of different thicknesses, it was possible to adjust the total laser intensity with a minimum profile deformation. In the ideal case, the Beer-Lambert law provides that:

$$I = I_0 \cdot 10^{-A} \tag{3.4}$$

where I_0 is the unfiltered intensity and A is the absorption coefficient of the single disc: these vary between $A \in [0.2, 4]$, and thanks to the presence of a double gear it was possible to stack two different discs onto the beam tray. The total absorbing coefficient is defined as $A = A_1 + A_2$, where $A_{1,2}$ are the single disk coefficient. It was also possible to transmit the beam unaltered, thanks to the presence of a free path (with no discs present).

3.1.2 The cuvette

A suitable container was required to hold the particle suspension: the incident beam was collimated (with an average diameter in the thousands of a nanometres range) inside a standard polystyrene (PS) cuvette with inner base dimensions of (10×10) mm and a height of 45 mm, for a total maximum volume of 4.5 ml. The optical path, when the cell is perfectly aligned, is $d = 10$ mm. The cuvette presented a very low absorption coefficient at $\lambda = 1064.2$ nm, and is therefore considered to be transparent.

The first scattering solution consisted of a water suspension of polystyrene spheres[1], with a diameter $2a = (0.34 \pm 0.01)\,\mu$m (the error refers to the standard deviation). The initial aim was to reach a concentration of $\rho_{V/V} = 0.1\%\,\text{ml/ml}$, deemed suitable for the experiment in order not to incur in multiple scattering phenomena: however, during the operations it was noted that the prepared solution presented a higher opacity than expected. This may be explained considering that the particles' container had been previously opened and, even if it had been refrigerated in advance, over time some of the particles may have agglutinated (this is an *ansatz*). In a light scattering experiment, an high polydispersity index makes the analysis more complex, due to the fact that multiple decays can be observed at the same time. In order to obtain a suitable scattering medium, after an appropriate dilution a new solution with a (calculated) density of one tenth of that of the stock was prepared and then transferred into the cuvette, which itself was covered with a layer of parafilm to prevent dust from entering; it was also necessary to ensure that no bubbles have formed inside the cuvette.

Because the correlation time of the first solution was too short for the camera to properly acquire a complete profile of the autocorrelation function, another one was prepared: this time, it consisted in a water-glycerol suspension of polystyrene particles[2], with a diameter of $2a = (1.28 \pm 0.04)\,\mu$m. 3 ml of the particle's aqueous solution, with a solid content of $10\,\% - \text{wt.}$, were added to 147 ml of almost pure glycerol in a test tube. Because now the solvent is a mixture of the two liquid, his viscosity is intermediate between those of the two separated.

[1] *Micro Particles*, batch PS-R-KM303
[2] *Micro Particles*, batch PS-R-L2537

The expected correlation time, obtained from [Eq. 2.31] taking into account [Eq. 2.3] with a fixed scattering angle $\theta = \pi/2$, follows:

$$\tau^{th.} = \frac{3}{8\pi}\frac{\eta a \lambda^2}{k_b T n^2}\left(\sin\frac{\theta}{2}\right)^{-2} \tag{3.5}$$

where η is the solvent viscosity, $T \sim 25\,^{\circ}C$ is the average laboratory temperature during the experiment, with $\lambda = 1064.2\,\text{nm}$ it resulted $n \simeq 1.33$ for water [11] and $n \simeq 1.46$ for glycerol [12]; regarding the spheres, the best estimate of the radius is the mean value $a = 0.64\,\mu\text{m}$.

3.1.3 The acquisition branch

In materials such as gels and glasses, the restructuring processes are usually spatially heterogeneous and intermittent in time, leading to a very different behaviour in different regions of the sample all at the same time. To spatially resolve the sample, in an imaging configuration a low-magnification image (in the specific experiment of a factor $G = 1.5$, as shown below) of the scattering volume is fed to a multi-pixel detector: the scatterers themselves couldn't be resolved, and the speckle pattern is generated from the superposition of the signals from all the particles in a localized sub-volume of the sample.

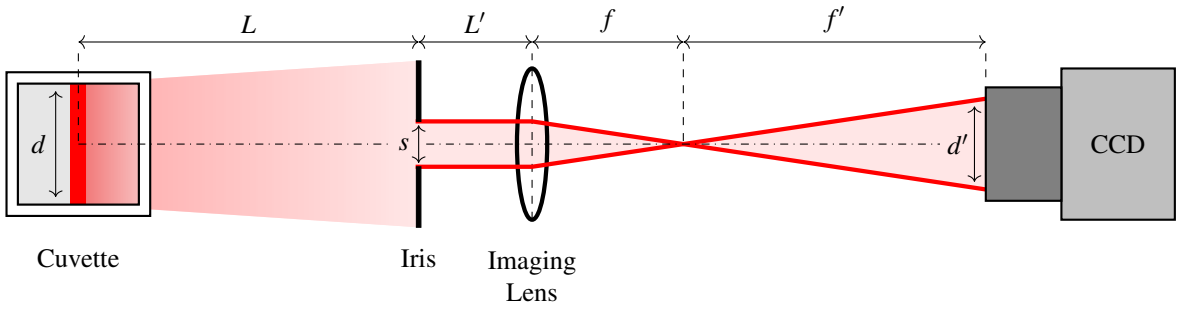

Figure 3.3: *Cross section of a simplified scheme of the acquisition branch (not to scale).*

In the geometry chosen for the setup, an iris was placed in before the imaging lens: by adjusting the pupil aperture it is possible to fix the Numeric Aperture of the lens, and thus the speckle size (as shown below). In the approximation that the scattered light does not diverge, the diameter of the light spot on the focal plane of the lens can be estimated with the pupil aperture s. However, referring to [Fig. 3.3], the iris and the lens were not on the same plane: the diaphragm is placed at a distance L from the scattering volume, separated by a distance L' from the lens. This could lead to the formation of a bigger spot onto the lens plane thus increasing the NA. In order to avoid this phenomena, as an experimental condition, it is necessary to make $L'/L \ll 1$, so that the maximum relative divergence on the lens plane:

$$\alpha = \frac{\delta s}{s} = \frac{d+s}{s}\cdot\frac{L'}{L} \ll 1 \tag{3.6}$$

where d is the optical path of the laser beam inside the cell. The iris diameter could later be corrected by a factor $s^\star = s\cdot(1+\alpha)$ so that $NA_{lens} \approx s^\star/(2f)$.

Consider now a *structured source* of size d, which scatters light due to the presence of particles of size $a \ll d$ comparable to the wavelength of the incident radiation, but too small to be optically resolved. In an imaging configuration, the speckles produced by this kind of source have a size determined by the optical system rather than the nature of the sample: this interesting consideration can be derived considering that the distance between two different speckles is given by a statistical average of the distances between adjacent regions of maximum and minimum brightness. The Rayleigh limit, generalized by the Abbe criterion (taking into account the presence of a single lens), allows to calculate the minimal separation between those regions. The resolving power is given by:

$$\frac{\delta x}{2} \approx J_1\frac{\lambda}{NA} \tag{3.7}$$

The dimension of a single speckle on the detector plane can be obtained as [13]:

$$\zeta \approx J_1\frac{\lambda}{s}\cdot z = J_1\frac{(1+G)}{2}\frac{\lambda}{NA} \tag{3.8}$$

where s is the pupil diameter and $z = f + f' = f(1+G)$ is the distance between the lens and the detector. The chosen imaging lens has a focal length of $f = 40\,\text{mm}$, while the iris aperture was set to $s = 1.5\,\text{mm}$: this corresponds to a theoretical speckle size of $\zeta^{th} \simeq 87\,\mu\text{m}$; from [Sec. 3.1.4], an average speckle linear span of about 6 pixels. Thanks to the reversibility of the imaging application, we have that the speckles on the detector are generated by a sub-volume in the sample with a size (referring to [Fig. 3.4]):

$$\zeta_0 \approx J_1 \frac{\lambda}{G \cdot s} \cdot z = \frac{\zeta}{G} \xrightarrow{G \to \infty} \delta x \tag{3.9}$$

where the factor G under the fraction compensates for the magnification. An interesting observation is given by taking the limit for an infinite magnification: the Rayleigh limit constrains the resolution, which asymptotically reaches a physical minimum.

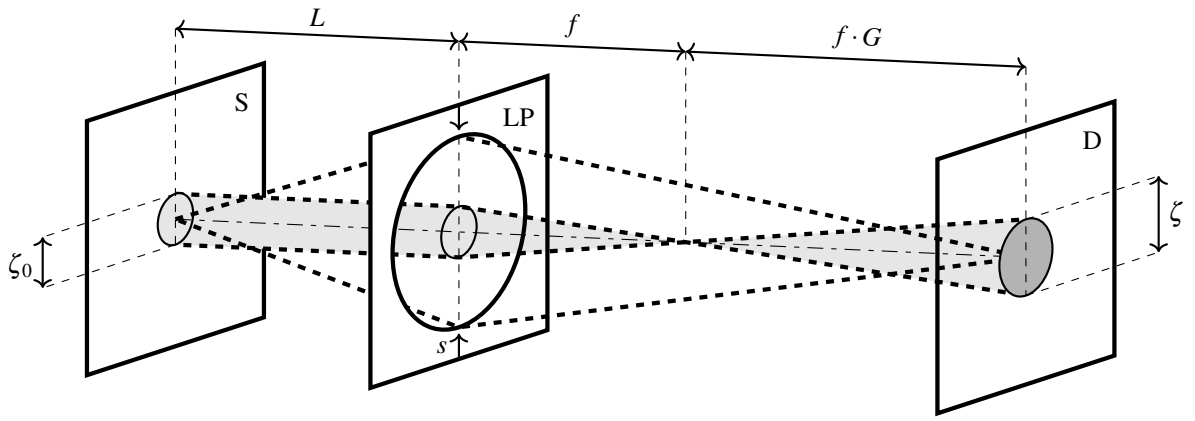

Figure 3.4: *The collective scattered field from a sub-region of size ζ/G on the Source plane 'S' creates a speckle of size ζ on the detector plane 'D', by feeding light through a narrowed lens positioned at 'LP' of size $s \ll d$ (not to scale).*

In all of the previous considerations the light source was supposed to be uniform; however, the scattering volume is not flat: indeed, we can approximate the illuminated region in the cell as a cylinder of radius r' (referring to the notation of [Fig. 3.2]) and length d. If we don't consider the projection optics between the scattering volume and detector, the size of a coherence area generated by a scattering volume with a transverse area $A = 2r' \cdot d$ can be approximated as [1]:

$$A_{coh} = \frac{(\lambda \cdot z)^2}{A} \quad \Rightarrow \quad l_{coh} = \frac{\lambda \cdot z}{l} \tag{3.10}$$

where l is the volume transverse dimension in a specific direction. Thus, upon increasing the global size of the scattering volume, the coherence area becomes smaller. As seen before, the speckle size given by an uniform scattering volume corresponds to the resolution limit given by the spacing of the interference fringes generated by waves coming from the opposite ends of a pupil; if instead we consider a cylindrical like scattering volume, different direction will present different correlation lengths. On the horizontal direction, because $d \gg s$ the speckle size will be determined by the intrinsic resolution of the setup. On the vertical direction, instead, the pupil size is comparable with the volume length $s \sim r'$: this means that on the lens plane the coherence length will be larger than the actual resolution limit. A rough estimate provides:

$$\zeta_V = G \cdot l^v_{coh} = G \cdot \frac{\lambda \cdot z}{2r'} \simeq 153\,\mu\text{m} \tag{3.11}$$

This results in rod-like speckles, with a different size according to the direction: globally they could be seen as ellipses with a size ζ on the horizontal plane and $\zeta_v \sim 2\zeta$ on the vertical. This elongation also depends on the coherence of the laser beam and on the coherence of the light itself: overall, the speckle pattern is given by a combination of many partial patterns.

Because the speckle pattern is given the total contribution of the sub-volumes within all the depth of field of the imaging lens, the third dimension only has the effect of selecting the number of the scatterers in the region considered. This affects the speckle brightness: moving along the vertical direction increases or decreases the number of illuminated regions in the transversal volume behind a coherence area, that follows the beam profile and is therefore Gaussian.

To improve the angular accuracy, the camera could be moved further away from the pupil, reducing the number of speckles on the detector and hence the statistical accuracy, or the iris could be slightly closed, with the same result. A way to deal with this problem would be an angle-dependent analysis; this could be achieved in two ways: by rotating the camera branch, focusing on a smaller region and varying the angle θ with the direction of propagation of the beam, or by making an accurate estimate of the momentum of the photons impinging on different pixels on the CCD. However, neither of these two approaches was used: an estimate of the maximum deviation from the mean value provides $\Delta\theta_{max} < 1.7°$, and so $\Delta q_{max}/q \sim 0.04\%$. This is considered to be small enough and thus neglected: from now on, the exchanged photon momentum can be considered a fixed value.

To adjust the pupil diameter, some considerations are necessary: the main limiting factor is the CCD sensitivity, which has a readout noise of $28 \div 38$ electrons in high gain mode, to which we have to add thermal and electrical noise as well as the signal from other light sources (see [Sec. 3.3.2]). If we assume that, on average, the flux from the scattering volume is constant in time and symmetric with respect to the rotation around the beam axis, a variation of the pupil diameter by a factor n causes a variation of the total transmitted power by a factor n^{-2}, drastically reducing the signal strength. It is necessary to find a compromise between the speckle size, the total signal power and the precision in the momentum selection.

In the previous considerations, it was assumed that the other optical component between the camera and the illuminated medium behave ideally: in particular, the square geometry of the cell allowed to negate any distortion of the scattered field from the refraction caused by the passage from the suspension to the cuvette wall and from the wall itself (for Polstyrene, the real part of the refractive index at λ is $n_{PS} \simeq 1.571$) to air ($n_{air} \sim 1$). To remove other spurious component, such as the light from other light sources and the eventual luminescence, a very narrow bandpass filter with a bandwidth of $(1064.0 \pm 1.5)\,\text{nm}$ at FWHM is inserted before the camera lens, cutting off unwanted light from reaching the sensor.

3.1.4 The camera

The acquisition branch of the setup has to be built to optimize the speckle pattern acquisition: the imaging configuration excluded the traditional *Avalanche PhotoDiodes* (APDs), in favor of a *Charge Coupled Device* (CCD) camera as detector.

Compared to the diodes, which are faster than the camera and can be used for real-time analysis, the CCD has a much higher sensitivity (as shown in [Fig. 3.5], at least 150 times better at the probe wavelength considering that standard silicon detectors have a $QE[1064\,\text{nm}] \sim 0.5\%$ [15]), as well as higher resolution and an unmatched low noise. Combined with the intrinsically high statistical accuracy of multi-speckle detection, this results in an improved performance of the detector configuration.

The CCD camera used was the *PSEL VGA* $15\,\mu m$ *InGaAs* infrared camera, preferred for its low dark current and an high quantum efficiency at the probe frequency ([Fig. 3.5]). The active area of the sensor measures $(9.6 \times 7.68)\,\text{mm}$ and consists of an array of (640×512) pixels; the camera has an ADC resolution of 14 bits and presents a 174 frames per second (fps) speed at full VGA resolution, with a minimum exposure time of $\delta t_{min} = 30\,\mu\text{s}$ (from *Photonic Science* [14]).

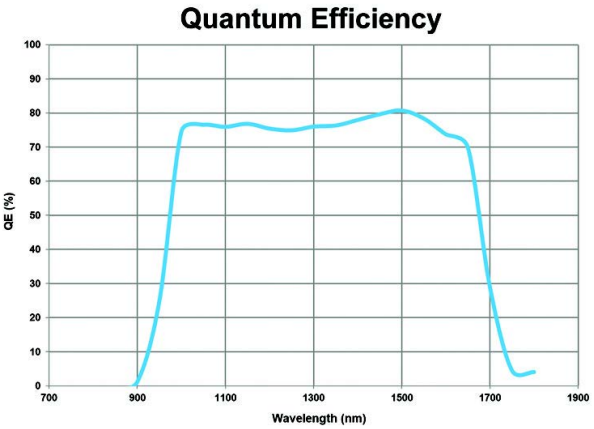

Figure 3.5: *Quantum efficiency as a function of wavelength for the CCD used, retrieved from [14].*

The collected signal is then analyzed by the correlator software, whose functioning will be further discussed in [Sec. 4.3.3].

3.2 Contrast

In DLS, the illuminated scattering volume behaves as a random source and produces a speckle pattern excibiting a coherence area A_c. Consider now a detector with aperture A (which, for a cell-type sensor such as the CCD used in the setup, is a single pixel area): the resulting output signal is proportional to the integral of the total incident

intensity (as explained in [Sec. 3.3.1]). For a given wavelength and scattering volume's position, the scaling factor between the coherence area (that corresponds to the average area of a speckle) and the detector area is:

$$N = \frac{A}{A_c} \tag{3.12}$$

If $N > 1$, more coherence areas will be present on the detector simultaneously: this is because different speckles are generated independently by different sub-volumes, each of which behaves randomly. In an acquisition time δt the detected power would be higher (compatibly with a larger sensor), but the overlap of different uncorrelated speckles only results in a constant signal baseline. To understand the effect on the autocorrelation function, it is useful to rigorously define the *contrast*:

$$K := \frac{\sigma\left[I(q,t)\right]}{\langle I(q,t)\rangle} \tag{3.13}$$

where $\langle I(q,t)\rangle$ is again the average intensity value as a function of the momentum q and $\sigma\left[I(q,t)\right]$ is its standard deviation. For a significant number of speckles on the sensor, the intensity fluctuation will follow a Poisson statistic: if $\langle I(q,t)\rangle \sim N$ thus $\sigma[I(q,t)] \sim \sqrt{N}$. This leads to the following limit:

$$\lim_{N\to\infty} K = N^{-1} \tag{3.14}$$

Increasing the number of speckles on the sensor results only in a loss of contrast; nonetheless, this is just an asymptotic law: for the opposite limit $K \to 1$ for $N \to 0$, due to the fact that a single speckle is coherent with itself, so selecting a smaller region does not result in any information loss concerning the single speckle coherence. In general, the *Siegert relation* presented at [Eq. 2.22] must be corrected as:

$$g^{(2)}(q,\tau) = 1 + f(N)\cdot\left|g^{(1)}(q,\tau)\right|^2 \quad ; \quad \text{where } f(N) \sim (1+N)^{-1} \tag{3.15}$$

$f(N)$ is also known as *degree of spatial coherence* of the scattered light and, if low, it affects the signal-to-noise ratio since it makes impossible to distinguish the homodyne autocorrelation function from its asymptotic value (refer to [Eq. 3.20]). The difference with the contrast is in their practical definition: K is a purely experimental quantity, while theoretically $f(N)$ depends only on the setup geometry and not by the scattering medium itself. Using [Eq. 2.6], it can be shown that:

$$\begin{aligned} f(N) = \lim_{\tau\to\infty}\left[g^{(2)}(0) - g^{(2)}(\tau)\right] = \frac{\langle I(q,t)^2\rangle - \langle I(q,t)\rangle^2}{\langle I(q,t)\rangle^2} = \frac{\left\langle\left[I(q,t) - \langle I(q,t)\rangle\right]^2\right\rangle}{\langle I(q,t)\rangle^2} = \\ = \left(\frac{\sigma\left[I(q,t)\right]}{\langle I(q,t)\rangle}\right)^2 = K^2 \end{aligned} \tag{3.16}$$

where [Eq. 2.7] was used for $f(N)$ to be defined positive. K can be expressed in terms of the normalized standard deviation of the intensity value, and so it can be evaluated even before the $g^{(2)}$. To obtain a high contrast, the coherence area should be considerably smaller than the detector aperture: with an imaging system we have the possibility to tune the effective size of the speckle by narrowing the lens with the iris diaphragm ([Sec. 3.1.3]). With the chosen setup configuration, the theoretical coherence factor (considering [Eq. 3.8, 3.11] for an estimate of the coherence area) is about $f(N)^{th} \simeq 0.98$; other factors reduces the contrast (as will be seen in [Sec. 3.3]), so that $0 \leq K^2 \leq f(N)^{th}$. Due to the numerous noise components, there is no reliable mean to actually estimate the parameter $f(N)$ a priori, leaving this only to the post-processing fitting of the autocorrelation function.

3.3 A priori noise analysis

Even without the experimental error contributions, there are intrinsic limits to the precision with which the properties of the system can be inferred. In particular, the signal-to-noise ratio can be affected by several factors that don't depend on the specific component used, but are inherited by the technique implemented in the analysis or deal with the quantum nature of light.

In this Section these factors will be identified, and their influence on the final setup briefly discussed. Among the many involved, it is possible to acknowledge two main sources of noise: the physical limits and the environmental contribution (mainly in the form of unwanted scattered light).

3.3.1 Discrete Correlation Function

In [Sec. 2.3], when defining the homodyne correlation function, it was assumed to be possible to measure the light intensity as a function of the time in a continuum manner. However, due to the discrete sampling time of the camera, a certain number of photons collected during a time interval δt is converted into a signal $s^j(t)$ proportional to the number of charge carriers $n^j(t)$ generated during the acquisition time. The total signal is thus given by an integral over the surface area of the local light intensity:

$$s^j(t) \propto n^j(t) = QE(\lambda)\frac{\lambda \varepsilon_0}{2h}\int_{S^j} d^2r \int_{t-\delta t/2}^{t+\delta t/2} dt'\, I\left(q(\vec{r}),t'\right) \tag{3.17}$$

where $QE(\lambda)$ is the quantum efficiency at a given wavelength (assumed uniform across the entire sensor) and $\vec{q}$ varies over the area S^j of the j-pixel. Operatively, a discrete version of the autocorrelation function called *count-autocorrelation function* can be defined as:

$$C^j(k) = \frac{1}{N-k}\sum_{i=1}^{N-k} s_i^j \cdot s_{i+k}^j \quad ; \quad \text{where } k = \frac{\tau}{\delta t} \tag{3.18}$$

where s_i^j is the signal registered by the j-pixel at the acquisition time $t = i \cdot \delta t$, proportional to the number of photons impinging the single pixel in a generic time interval $[(i-1/2)\delta t;(i+1/2)\delta t]$. Unlike the continuous-autocorrelation function, the discrete one requires an appropriate normalization dependent from the lag time (in this case, from k), to compensate on the finite number of bins analyzed. This function approximates to the true autocorrelation function whenever $\delta t \ll \tau_c$, so that the intensity has a quasi-constant value in the time interval of the frame acquisition $I(q,t+\delta t) \approx I(q,t)$. In the Gaussian approximation (refer to [Sec. 2.3.1]), from Jakeman and Pike [16], it is possible to reduce the calculation to the $g^{(2)}$ to [17]:

$$g^{(2)}(q,t) \approx C(t) = \langle n \rangle^2 \left[1 + f(N)\exp\left\{-\frac{2t}{\tau_c}\right\}\right] \tag{3.19}$$

where $f(N)$ is again the *degree of spatial coherence* of [Eq. 3.15] and $\langle n \rangle$ is the average number of photons detected; an opportune normalization allows to get rid of this term. From experimental data fitting, it is possible to extract the relaxation time as well as the other parameters.

It is now possible to estimate the error contribution introduced by the finite time averaging in the calculation of the correlation time: there are only $T/(2\tau_c)$ independent samples in the correlation function, where T is the averaging time (i.e. the total acquisition time). Since the error should be proportional to the inverse square root of the number of experimental points and to the distance of the homodyne autocorrelation function from its asymptotic value ($g^{(2)}(q,t) \xrightarrow{t\to\infty} 1$), it is possible to roughly approximate (following Berne and Pecora [1]):

$$\sigma_T(t) \approx \sqrt{\frac{2\tau_c}{T}} \cdot \left(g^{(2)}(q,t) - 1\right) \tag{3.20}$$

To reduce this error, it is necessary to average over many correlation times. The total signal to noise ratio can be calculated from a series expansion of the autocorrelation function:

$$\frac{S}{N} = \sqrt{\frac{T}{2\tau_c}} \tag{3.21}$$

3.3.2 Environmental noise

Of all the contributions to the total noise, the environmental components play a preponderant role in the calculation of the autocorrelation function. These generate systematic effects that often presents the behaviour of a different dynamic process: a subsequent estimate of the decoherence time may be affected by them.

First, light intensity fluctuations heavily affects the calculation of the autocorrelation function (due to the required normalization): the laser itself has nominal power stability $< 2\%$ in the operational regime, with a total noise of less than 0.1% RMS. The main source of this component is due to the statistical nature of the light scattering: the total intensity from all the coherence areas slightly fluctuates over time, resulting a variation of the total intensity from the sample between a frame acquisition and the next. A simple way to mitigate this phenomenon is to normalize each frame to the average light intensity: when calculating the autocorrelation function, it is ensured that each coherence area presents the same average intensity for every t.

The main noise component, with a global effect on the scattered field, is the presence of unwanted signals, either from unwanted scattering or from background noise. This introduces a systematic error in the calculation of the homodyne autocorrelation function, by lowering the overall contrast (introduced in [Sec. 3.2]) and represents the main limit on the signal-to-noise ratio for the "real" experiment. In addition, the presence of a small amount of unscattered light, due to reflections, can lead to the measurement of a second exponential decay in the homodyne autocorrelation function, with an amplitude proportional to the local oscillator intensity.

When a flow forms in a fluid, for example due to convection, it induces a directional pattern in the motion of the suspended particles, which can affect the scattered field with a transnationals component. These movements can be caused by several factors: external thermal fluctuations, which induce a thermal gradient in the cell; external irradiation, caused by the laboratory light sources and neglected thanks to the experimental conditions that ensured minimal interference; and finally the local heating caused by the laser absorption, which cannot be eliminated and constitutes the main contribution to the thermal noise. This became relevant at higher laser powers, leading to a dynamic that is no longer describable as a simple Brownian motion as in [Sec. 2.5]: a more extensive work is provided by Gabriel [18], and require the introduction of a power factor β that "stretches" the exponential. Air flows in the free path of the lasers, which scatters light due to convective motion, can also have a measurable effect on the detector: the (supposedly) high contrast obtained allowed this source of noise to be ignored.

Unwanted scattering was also caused by the presence of particulate in the cuvette: impurities, dust, air bubbles (especially at higher laser powers) or foreign materials can cause disturbance in the calculations of the correlation function due to the strong scattered field intensity related to their dynamics (diffusive and ballistic) in the cell. As a result, a second exponential decay collectively generated by the impurities may be observed in the homodyne autocorrelation function. The sample preparation was then crucial to remove this possible noise contribution, and is described in [Sec. 3.1.2]. Dust on the optically passive components, especially on the imaging lens, could also cause artefacts on the detector.

Another source of noise is caused by mechanical vibrations: if the laser or the camera vibrates with respect to the cuvette, the images formed on the CCD will "oscillate" with a characteristic time that in most cases satisfies $t_{vibr.} \gg \delta t_{sampling}$. In a single frame, these contributions can be neglected, but in consecutive images the pixel alignment with respect to the speckle pattern will no longer be the same, leading to an induced faster decaying in the correlation function as seen from a single pixel. To limit this problem, the setup was placed on a special optical table: this was built with a series of air pistons that decoupled the laboratory vibrations (e.g. induced by the operators walking) from the setup itself.

Finally, unwanted noise light and luminescence were largely shielded by the bandpass filter in the camera branch [Sec. 3.1.3], whilst thermal and electric noises were reduced by the camera's internal cooling system (the camera internal temperature remained stable at $-32°C$ for the duration of the experiments).

4

Characterisation measurements

The main goal of this Thesis work is to built and test the whole setup, and specifically to prove that all of the components behave as expected. Misalignments, aberrations and other factors could easily compromise the result obtained by the analysis: the tests are intended to verify that, with a simple dynamics, the results obtained are correct. It has to be reminded that the final setup will be different, with the addiction of numerous other components such as beam-splitters and an entire new pump branch. Specifically, the importance of the imaging configuration will be proven: if the dynamic in the cuvette is not uniform the autocorrelation function present non-negligible anisotropies both in space and in time. This allows to study inhomogeneities in the behaviour of the sample, which are fundamental in amorphous material like glasses: if this capacity is compromised, it could lead to erroneous results.

This last Chapter presents the first tests performed on the setup, using the configuration illustrated in [Sec. 3.1] and shown in [Fig. 3.1]. First, some brief consideration on the imaging configuration will be addressed, together with some additional information about the the camera settings; then the acquired data-sets will be presented, analyzed and discussed.

4.1 Collimator and beam expander alignment

The collimation of the laser was a delicate operation, due to the importance of a focused source for the experiment and the difficulty encountered in the physical operation. In [Sec. 3.1.1], it was defined as radius of the beam r the distance at which, from the propagation axis, the laser intensity was superior to the 2σ value: although the tails of a Gaussian function never actually reach zero, for the purposes of the following discussion the "edge" of a beam is considered to be the radius.

In order to verify the correct alignment of the collimator, a *Thorlabs BC106N-VIS/M* beam profiler was used: it presented a (1360×1024) pixels sensor, with a 12 bit resolution; each pixel has a size of $6.45\,\mu$m [19]. As will be explained in [Sec. 4.3], the output powers used for the laser were $P_{laser} = (200; 500)$ mW: the collimation procedure was performed measuring the beam size at those two power values. The measurements were performed at two specific distances $z = (15; 40)$ cm: the first is compatible with the optical length between the collimator and the cuvette; and ~ 40 cm is the calculated Rayleigh length [20] which, for an ideal collimated Gaussian beam, represents the distance along the propagation direction where the area of the cross section doubles with respect to the waist. An example of the obtained images is shown at [Fig. 4.1]; the measurement results after the collimation are presented in [Tab. 4.1].

For each distance and output power, multiple data-sets were acquired in the same condition allowing to obtain an acceptable error estimate. The halo around the beam is generated by the lens of the beam profiler, as well as the "striped" pattern; weak tiny Airy disks are also visible, caused by the presence of dust on the lens.

It is possible to notice that the beam is not perfectly collimated: this slightly overcollimation allows us to increase the power density, as well as to avoid an excessive divergence of the beam inside the cuvette. It is also relevant that different powers correspond to different beam sizes, which is an unexpected effect with respect to the considerations about the laser in [Sec. 3.1.1]. A good beam symmetry is also important, as stated in [Sec. 3.1.1]; for almost all data-sets, the two estimates of the beam size are compatible within the 3σ: for $z = 15$ cm, which is near the true laser optical path, the asymmetry is negligible.

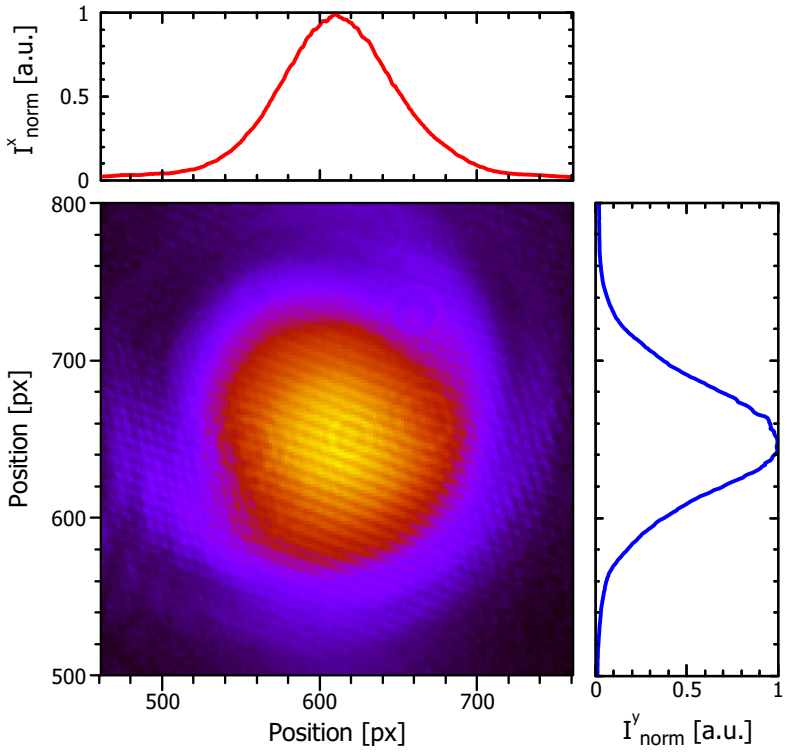

Figure 4.1: *Map of the normalized light intensity of the beam profile with a nominal output power of* 200 mW *at* $z = 15$ cm *from the collimator. The map scale is logarithmic: warmer color indicates an higher intensity. The projection on both axis are shown.*

P_{laser} [mW]	z [cm]	r'_x [μm]	σ_x [μm]	r'_y [μm]	σ_y [μm]	$\mathscr{T}(r'_x, r'_y)$
200	15	*890*	*7*	*898*	*5*	*0.9*
	37	*357*	*2*	*351*	*1*	*2.8*
500	15	*784*	*2*	*788*	*5*	*0.7*
	37	*380*	*2*	*402*	*3*	*5*

Table 4.1: *Estimate and relative error of the beam size as a function of the distance from the collimator and the laser output power; the Gaussian compatibility* $\mathscr{T}$ *between the two estimates of the beam radius is also displayed. The notation* $r_{x,y}$ *refers to the beam profiler's reference system.*

4.2 Final setup adjustments and camera configuration

The final alignment of the camera branch was performed immediately before the acquisitions, in order to correctly center the imaging system on the cuvette. The probe branch alignment was performed through the use of fluorescing alignment disks, that ensured the correct positioning of the beam respect to the cell. All of the optical components, such as the optical fibre, the lenses and the absorber, as well as the cuvette's wall, absorbed a fraction on the total impinging power: an estimate provided that the power loss was about $(15 \div 20)\%$ of the total. After a proper laser stabilization, the absorber was rotated to obtain the desired laser intensity on the cuvette: this allowed us not to modify the laser power output for the majority of the acquisitions, thus guaranteeing a better stability ([Sec. 3.1.1]).

The cuvette was then aligned into its final position, using the feedback from the camera itself and the power meter to check the correct position. All measurements were conducted in the absence of external lighting supplies, so that the light noise was reduced as much as possible. To eliminate eventual fixed noise sources, and to correct eventual burned pixels, a set of *dark* images were acquired with the laser off for each measurement and used by the camera software to correct the final acquisitions frames. Also, the camera was provided with a built-in *flat-field* correction.

The camera was then configured to acquire the images with an appropriate gain, and the acquisition time between an image and the next was set at $\delta t = 5$ ms for the first group of data-sets, collected using the water

suspension, and $\delta t = 20\,\text{ms}$ for the glycerol solution. The readout time [14] brought the acquisition frequency to $f \sim 115\,\text{fps}$ and $f \sim 50\,\text{fps}$, respectively. Between an acquisition and the next, for several seconds the laser was blocked (with an internal shutter), in order to allow the cuvette to cool off and reach the laboratory temperature before the successive measurement.

4.3 The data-sets

A total of 7 data-sets were acquired for the first test sample, each one with a different incident beam power $P = (10;20;30;40;50;100;500)\,\text{mW}$ at full VGA resolution. An example of the acquired frames is presented at [Fig. 4.2].

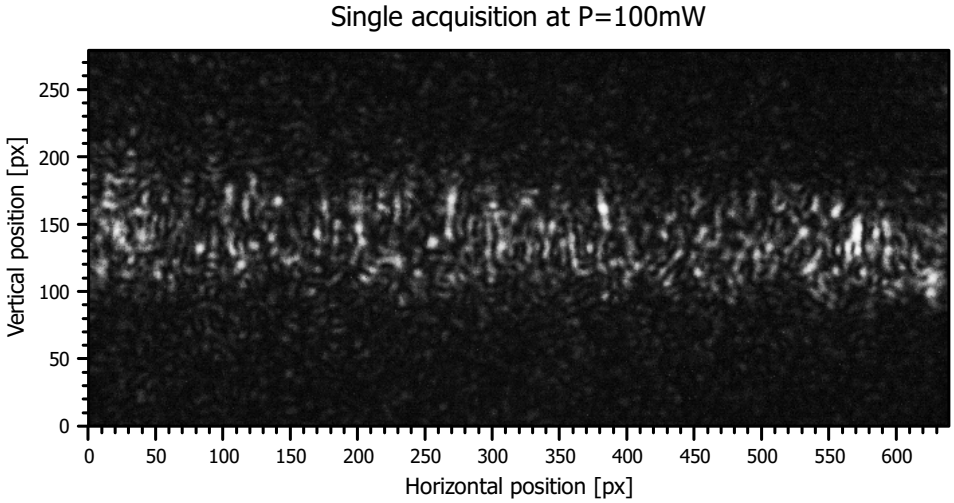

Figure 4.2: *Raw frame acquisitions with the first test sample at* $P = 100\,\text{mW}$. *The beam direction is left to right.*

The majority of the scattered light comes from the beam center, compatibly with the considerations of [Sec. 3.1.3]; however, it is interesting to observe that also weakly illuminated regions produces a not negligible speckle pattern. For the acquisitions at $P = (100;500)\,\text{mW}$ the system dynamics can no longer be considered stationary, due to the triggering of convective motions in the cuvette ([Sec. 3.3.2]): in this situation the coherence time changes as a function of the time.

In the "external" regions, the noise contributes with a non-negligible component with respect to the brightness of the speckle pattern: for the sets acquired with a low incident power, this noise represent the limiting factor in the contrast resolution (see [Sec. 3.2]). Also, reflection caused by the cuvette walls are visible on the image left and right borders. For those reasons, it was necessary to select a *Region Of Interest (ROI)* where to compute the data analysis, in order to obtain more accurate results. To increase the laser stability, the measurement under $\leq 100\,\text{mW}$ were all performed with the same output power of $P_{laser} = 200\,\text{mW}$, using the absorber to reduce the effective light intensity (as remembered in [Sec. 4.2]). The measurement at $P = 500\,\text{mW}$, instead, required the laser path to be completely unobstructed (and consequently $A = 0$, from [Sec. 3.1.1]).

For the glycerol suspension, instead, 3 measurements were performed at $P = (1;10;100)\,\text{mW}$ with a reduced ROI: those sets were used to calculate the time autocorrelation function, while the previous helped to determinate the global behaviour of the setup.

4.3.1 Data analisys

In the original *Time Resolved Correlation* scheme [21, 22], Cipelletti and coworkers proposed a method to test the dynamics of materials which present a temporally heterogeneous evolution, such as gels and soft-matter materials in general [23, 24]. Using a camera, they took pictures of the speckle field scattered by the sample at regular intervals, measuring the correlation as a function of the time; the degree of correlation is calculated according to:

$$c(q,t,\tau) = \frac{\langle I^j(t) I^j(t+\tau)\rangle_q}{\langle I^j(t)\rangle_q \langle I^j(t+\tau)\rangle_q} - 1 \tag{4.1}$$

where $I^j(t)$ is the light intensity on the j-th pixel at time t, and $\langle \ldots \rangle_q$ represents the spatial average on an appropriate set of pixels corresponding to the same q-value. In the experiments, conducted in a *strong multiple*

scattering regime [25], each pixel collects light coming from the whole scattering volume: every speckle carries information about the behaviour of the whole sample, making the multi-speckle analysis a very powerful tool thanks to the high statistics which are obtainable. In a regime of *single scattering*, this technique allows to spatially explore the sample (as described in [Sec. 3.1.3]), making it possible to detect spatial heterogeneities by means of measurements of space and time resolved correlation functions: material like glasses can be studied with this method, providing extended information on the sample's restructuring as a function of the position and the time.

The autocorrelation function can be obtained as:

$$g^{(2)}(q,t,\tau) - 1 = \langle c(q,t,\tau)\rangle_T \tag{4.2}$$

where now the brackets represent the time average. In this final Section, the entirety of the data analysis will be presented, mainly focusing on the proper functioning of the imaging system and the overall quality of the data acquired.

4.3.2 Contrast and intensity distribution

It is relevant, in order to test the sensibility of the setup, to investigate the light dispersion in the intensity domain. The first group of data-sets was used to compute an extended analysis on a great number of pixels, resulting in a very high precision statistic. For all subsequent considerations the dynamics in the sample is supposed to be uniform: however it will quickly become clear that it is not possible to neglect spatial inhomogeneity effects.

Regarding the intensity, there are many factors that influence its probability density distribution; thanks to Goodman [4] it is possible to show that, for unpolarized speckles, it takes the form:

$$\rho^{th}(I) = \begin{cases} \langle I\rangle^{-1} \cdot \exp\left(-\dfrac{I}{\langle I\rangle}\right) & ; \quad \text{if } I \geq 0 \\ 0 & ; \quad \text{otherwise} \end{cases} \tag{4.3}$$

Where $\langle I\rangle$ represents the intensity mean value. This relation however is valid only for speckles generated by a uniform source in absence of external noise: effects like the finite pixel size of the CCD, the camera detector dark current and amplifier noise, background radiation, polarization effects, vibrations, turbulence effects, and the finite line-width of the laser beam could have contributed the the intensity PDF. Specifically, if we consider a global noise probability density distribution, the observed $\rho(I)$ can be expressed as [26]:

$$\rho(I) = \rho^{th}(I) * \rho_{noise}(I) \tag{4.4}$$

where the asterisk represent the convolution.

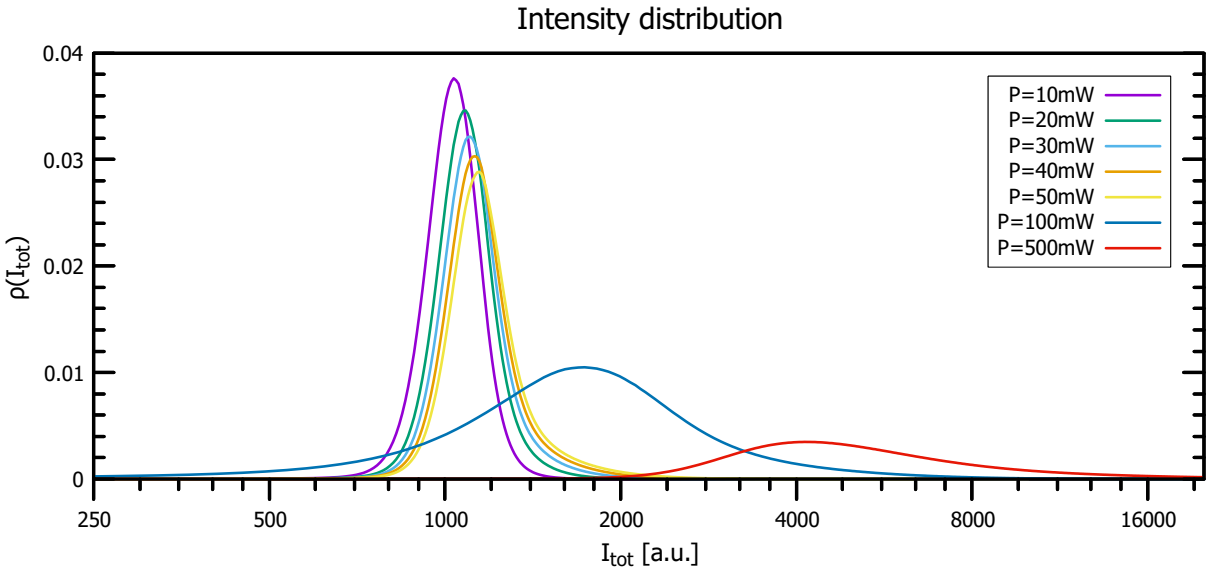

Figure 4.3: *Probability density distribution (normalized) as a function of the intensity at different values of the impinging power* P.

The presence of low intensity noise modifies the profile of [Eq. 4.3] to a peaked PDF curve with an exponential tail for higher intensity values; from the central limit theorem applied to the noise, the $\rho_{noise}(I)$ should be a Gaussian: in this hypothesis the shape of the PDF is an Exponentially-Modified Gaussian distribution (EMG). If the system presents non-negligible multiple scattering phenomena other decays could be observed. A graph of the calculated intensity distributions on the raw data for the water-suspension test sample is shown at [Fig. 4.3]. For $P = 10\,\text{mW}$ the distribution is almost Gaussian, as expected, while for higher values it become progressively more asymmetric compatibly with [Eq. 4.4]: [Eq. 4.3] is not sufficient alone to describe the experimental data. However, if an opportune correction for the "dark counts" is applied, it is possible to remove a consistent portion of the noise; this will be necessary for the final utilization of the setup.

From [Eq. 3.13], it was possible to evaluate the contrast as a function of the vertical coordinate remembering that, from [Sec. 3.1.3] and [Fig. 4.2], points with the same y-coordinate feeds on the same light intensity. Moving along the CCD it was possible to measure the variation of the contrast, as shown in [Fig. 4.4].

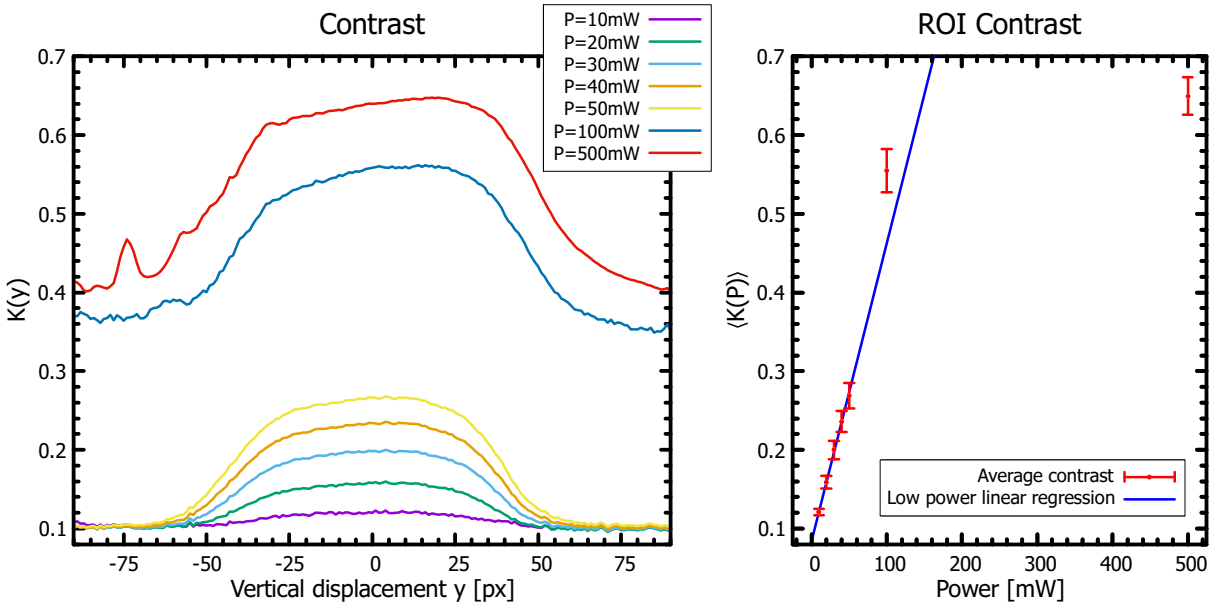

Figure 4.4: On the left, *average contrast as a function of the vertical displacement from the probe beam center.* On the right, *corrected average contrast in the selected ROIs and relative error; a linear interpolation for* $P \leq 50\,\text{mW}$ *is provided.*

Inside the beam the contrast is almost uniform: this behaviour is compatible with a system where the illuminated regions provide a speckle pattern different from the random noise visible in the "dark" zone; those estimates helped selecting the ROI for the data analysis. For $P = (50 \div 100)\,\text{mW}$, the contrast baseline rises from 0.1 to 0.38: between those two sets, it was necessary to change the camera gain in order to maximize the signal without saturating the CCD; the difference is compatible with that of the theoretical readout noise [14].

The analysis of the average contrast in the selected ROIs allows us to study the sample response to the impinging light beam; as a function of the power, the contrast follows a linear trend for $P \leq 50\,\text{mW}$: for those data, the linear regression $K(P) = a + b \cdot P$ provides an intercept value $a = (83 \pm 1) \cdot 10^{-3}$ that is not compatible with zero, coherently with the presence of the noise. For higher values of P, a more accurate noise subtraction could remove the non-negligible component that distorts the trend, thus providing more information for these power regions.

4.3.3 Autocorrelation

In this Section, the autocorrelation theory will be finally used on the data-sets to extract information about both the imaging configuration and the system behaviour: the goal of this discussion is to show that the setup allows to conduct a correct analysis, with the prospect of studying spatially inhomogeneous samples with a reduced acquisition time. In *Photon Correlation Imaging* every pixel act as an independent detector, thus the camera is able to perform Dynamic Light scattering measurements simultaneously an a very large number of speckles.

Due to different speckles being uncorrelated ([Sec. 2.1]), and considering that a CCD single pixel only feeds on light from a coherence region [Sec. 3.1.3, 3.2], the autocorrelation of light intensity performed on the sensor

area would provide an estimate of the speckle size. A rigorous definition is:

$$g^{(2)}(t,\vec{x},\vec{\Delta}) = \frac{\langle I(t,\vec{x})I(t,\vec{x}+\vec{\Delta})\rangle_r}{\langle I(t,\vec{x})\rangle_r^2} \tag{4.5}$$

where $\langle\ldots\rangle_r$ is the spatial average and $\vec{\Delta}$ is the spatial displacement vector. In principle, if the dynamic is spatially inhomogeneous, the $g^{(2)}$ depends on the starting point; however, if the sample is homogeneous the spatial average could be extended on the entire sensor. This expression only takes advantage of the multi-speckle statistic and does not consider multiple acquisition; if the sample behaviour is homogeneous over time, it is possible to evaluate:

$$g^{(2)}(\vec{x},\vec{\Delta}) = \langle g^{(2)}(t,\vec{x},\vec{\Delta})\rangle_T \tag{4.6}$$

where $\langle\ldots\rangle_T$ is the temporal average, and now the autocorrelation function does not depend on the specific frame (thus the acquisition time t). Due to the fact that the speckle pattern is co-oriented with the CCD axis ([Fig. 4.2]), and from he consideration of [Sec. 3.1.3] about the speckles dimension, it is only interesting to observe horizontal and vertical displacement: this translates in $\vec{\Delta} = (\Delta,0)^t$ or $\vec{\Delta} = (0,\Delta)^t$, where $(\cdot,\cdot)^t$ indicate the vector transpose and $\Delta = |\Delta| \in \mathbb{N}$. From Goodman [4], in an imaging system the autocorrelation function of the speckle intensity pattern consists of a constant term plus the squared modulus of the normalized Fourier transform of the intensity transmittance of the lens pupil:

$$g^{(2)}_{th}(r) = 1 + 4\left|\frac{J_1(r/l)}{r/l}\right|^2 \quad ; \quad \text{where } l = \frac{\lambda z}{\pi s} \tag{4.7}$$

where J_1 is the first order Bessel function of the first kind, r is the displacement, and all the other quantities are defined in [Sec. 3.1.3]; theoretically, this expression is independent from the aberration associated with the pupil. To meet the experimental data, the second term of [Eq. 4.7] should be corrected for the image contrast and the noise, with contribute with its own spatial autocorrelation.

Those considerations are only valid on the horizontal axis, where the speckle pattern forms because of the presence of a pupil whose dimension is limited by the diaphragm aperture. From [Sec. 3.1.3] it is possible to derive that, on the vertical axis, the speckles size is constrained by the illuminated volume's shape: for all of the sets acquired with the same gain (refer to [Sec. 4.3.2]) the $g^{(2)} - 1$ reaches the first minimum at (approximately) the same position; those points mark the speckles size on the vertical axis, and represents the limits of the Rayleigh diffraction projected by the pupil. By fitting the spatial auto correlation functions, horizontal and vertical respectively, it was possible to evaluate the speckles dimension. The results are shown at [Fig. 4.5].

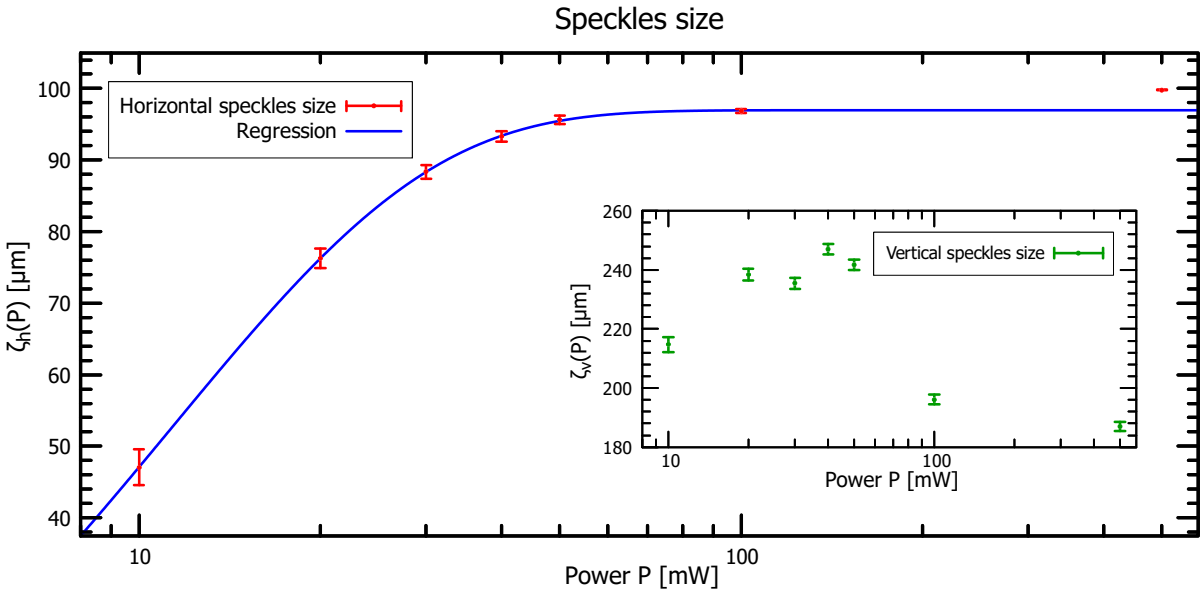

Figure 4.5: *Speckle size on both axis as a function of the power; the conversion factor from pixels to micrometers is the CCD pixel size [14]. An exponential regression for the horizontal axis at $P \leq 100\,\text{mW}$ is provided.*

The horizontal speckle size follows an exponential trend for $P \leq 100\,\text{mW}$, explained by the presence of the noise that affects the low power acquisitions: "darker" speckles will appear smaller due to the convolution with

the noise intensity profile. The plateau represents the theoretical limit given by the imaging resolution: the exponential regression $\zeta_h(P) = a + b \cdot \exp(-P/\xi)$ returns an horizontal speckles maximum size given by the parameter $a = (96.95 \pm 0.09)\,\mu$m, greater than the previous estimates. The discrepancy of the point at $P = 500$ mW could be explained by convective motions inside the cuvette ([Sec. 3.3.2]), which displays the scattering sub-region originating a speckle during the acquisition time, resulting in a bigger coherence area. It is immediately possible to notice that $\zeta_v \sim 2\zeta_h$, as calculated in [Sec. 3.1.3]: the average value for the vertical size of the speckles is $\overline{\zeta_v} = (0.22 \pm 0.03)$ mm. The speckles are bigger than what previously estimated, but the imaging system showed to work as intended.

The last test was intended to verify that the sample dynamics agrees with the predictions of [Sec 3.1.2]. To do this, it was necessary to calculate the time autocorrelation function as defined in [Eq. 2.10] and than "disceretised" in [Eq. 3.18]; rigorously, [Eq. 4.2] provides the best estimation method: if we consider that each single pixel feeds on a single speckle (from [Sec. 3.1.3] and [Sec. 3.1.4]), it is possible to estimate the single pixel autocorrelation function and then provide a spatial average. Operatively, it is convenient to define:

$$g^{(2)}(q,t,\tau) - 1 = \left\langle \frac{\langle I^j(t) I^j(t+\tau)\rangle_T}{\langle I^j(t)\rangle_T \langle I^j(t+\tau)\rangle_T} \right\rangle_r \tag{4.8}$$

with the meaning of the averages explained above. If the dynamics is homogeneous in time, the quantity inside the external brackets becomes the total single-pixel autocorrelation function; the average on the entire selected ROI, in a spatially homogeneous medium, allows us to take advantage of the multi-speckle higher statistic reducing the total error. However, if the medium exhibits marked anisotropies, this becomes a tool to study different dynamic processes at the same time. For the system considered in this experiment the homogeneous hypothesis will be considered to be valid, thus the $g^{(2)}$ will be considered independent from the start time and the single pixel impinging momentum q over a specific sensor area: the spatial integration is performed on the entire selected ROI.

The calculated autocorrelation functions on the 3 data-sets acquired for the second test sample is presented in [Fig. 4.6], where $g^{(2)}(q,t) - 1$ is ri-normalized for the contrast. The sets consisted of $N = 3000$ single frames, for a total acquisition time of $T = N \cdot \delta t \simeq 60$ s (from [Sec. 4.3]). The presented calculations were performed on all the data and clipped at $t = 25$ s, due to the presence of a "noisy tail" caused by the the smaller number of data-points in the averaging process for bigger values of τ (as highlighted in [Sec. 3.3.1] and [Eq. 3.18]).

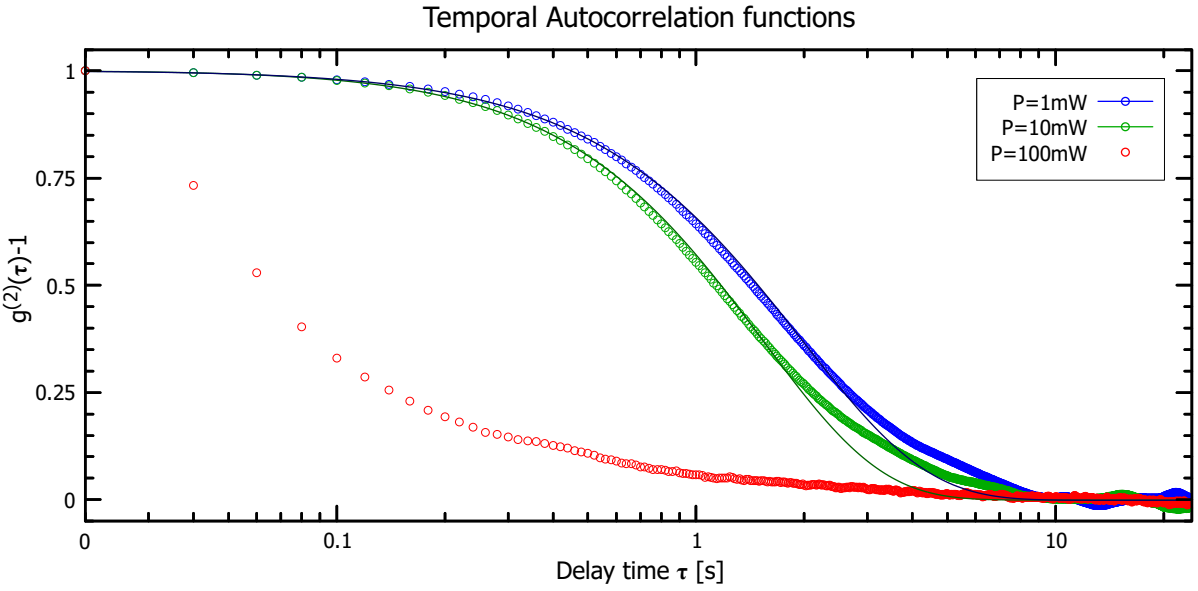

Figure 4.6: *Normalized time autocorrelation functions as a function of the delay time for the glycerol sample; interpolations for* $P = (1;10)$ mW *are also displayed.*

The acquisition for $P = 100$ mW presented a strong decorrelation, compatible with both the induced convective motion in the cuvette and a strong noise baseline that we observed. It is also possible to see multiple decays, that indicate a complex dynamics which can no longer be described as a simple Brownian motion. Slope changes are present in both the other acquisitions, which are also probably generated by the laser heating or by other relaxation phenomena that have not been considered.

Theoretically, the autocorrelation function should follow the corrected *Siegert relation* of [Eq. 3.15]: by fitting those data, it was possible to obtain the correlation time τ; a possible error estimate for the data point is given by

[Eq. 3.20] using [Eq.3.5] for a theoretical value of the correlation time. For the last set, instead, a more precise measurement is given by [Eq. 2.9]; the results are shown at [Tab. 4.2].

P[mW]	τ**[s]**	σ_τ**[s]**
1	*6.76*	*0.05*
10	*6.22*	*0.07*
100	*0.139*	*0.001*

Table 4.2: *Estimate and relative error of the coherence time as a function of the power.*

As expected, with an higher impinging power (and, consequently, an higher local temperature of the glycerol solution), the correlation times is smaller than what initially expected. Using the τ estimates obtained for $P = (1;10)\,\mathrm{mW}$, if we suppose that the temperature change is small compared to its absolute value, it is possible to calculate an experimental solution viscosity: by inverting [Eq. 3.5] it results an average value of $\eta \simeq (0.33 \pm 0.02)\,\mathrm{Pa}\cdot\mathrm{s}$, with $T \sim 25°C$ as the average laboratory temperature during the experiment. The pure glycerol viscosity is $\eta^{th}_{glyc} = (0.971 \pm 0.006)\,\mathrm{Pa}\cdot\mathrm{s}$ at $T = 25°$ [27]: the lower experimental value is compatible with the presence of water that was absorbed by the glycerol (a theoretical concentration of approximately $95\,\% - \mathrm{wt.}$ is consistent with the preparation of the sample [28]). This estimate is not accurate, and only serves the purpose of verifying that the acquired data are compatible with the dynamic process observed.

5

Conclusions

Photon Correlation Spectroscopy is a technique that allows to perform Dynamic Light Scattering experiments on a broad variety of materials, probing complex and heterogeneous dynamic process that other techniques cannot resolve. Setups built to study materials via PCS, despite being conceptually very simple, require a fine design and a complex procedure of calibration and characterization, which involves different tests in various conditions. The analysis of the speckle pattern, created by the superposition of the electric field from all the sample, allows us to infer on the system dynamics both in space and in time, and specifically on the behaviour of different spatially correlated volumes in the scattering medium.

The introduction of DLS theory allows to understand how a medium with non-negligible gradients in his dielectric constant behave when a light beam is scattered by those irregularities, and lays the foundations to the homodyne autocorrelation method and the possibility to obtain information about the sample behaviour. The practical application to the Brownian particles diffusion's model shows how the microscopic structure of a medium can be extracted by an analysis of his scattering pattern.

In the construction of the setup, the choice of components used was heavily influenced by the necessity to prevent or exclude various noise components, ahead of the successive analysis performed on the acquired data. Some issues were encountered during the assembly and the alignment of the setup itself, which required appropriate estimations in order not to incur erroneous results. The imaging configuration serves two important purposes: it allows to tune the effective size of speckle, by the use of a simple iris diaphragm, and with the same mechanism allows to obtain a spatially resolved image from the illuminated sample. A good setup calibration and optical alignment are mandatory to achieve consistent results.

A first characterization of the setup, realized through the use of test samples, completes the Thesis work: experimental PCS requires a rather complex and extensive analysis to be performed, always keeping in mind the underlying theory behind the observed dynamics. Upon completion of this project, I have acquired knowledge of constructing an optical setup and the theory behind coherent radiation scattering.

The concepts in this Thesis came from very different disciplines and many contributors, some of them which I have not had the opportunity to quote directly such as M. Giglio and coworkers [29, 30] and R. Piazza [31, 32], which works I took inspiration on.

Bibliography

[1] B. J. Berne; R. Pecora. *Dynamic light scattering. With application to Chemistry, Biology and Physics*. 2nd ed. New York: John Wiley & Sons, Inc., 2000. ISBN: 9780486411552.

[2] A. Einstein. "Über die von der molekularkinetischen Theorie der Wärme geforderte Bewegung von in ruhenden Flüssigkeiten suspendierten Teilchen". In: *Annalen der Physik* 322.8 (Jan. 1905), pp. 549–560. DOI: 10.1002/andp.19053220806.

[3] A. J. F. Siegert. *On the fluctuations in signals returned by many independently moving scatterers*. Report; 465. Cambridge, Mass: Radiation Laboratory, Massachusetts Institute of Technology, 1943. OCLC: 551981481.

[4] J. W. Goodman. "Speckle Interferometry". In: *Laser Speckle and Related Phenomena*. Ed. by J. C. Dainty. Vol. 9. Topics in Applied Physics. Berlin, Heidelberg: Springer, 1975. ISBN: 9783662432051. DOI: 10.1007/978-3-662-43205-1.

[5] P. Zakharov; S. Bhat; P. Schurtenberger; F. Scheffold. "Multiple-scattering suppression in dynamic light scattering based on a digital camera detection scheme". In: *Applied Optics* 45.8 (Mar. 2006), p. 1756. DOI: 10.1364/ao.45.001756.

[6] R. Zwanzig. "Time-Correlation Functions and Transport Coefficients in Statistical Mechanics". In: *Annual Review of Physical Chemistry* 16.1 (1965), pp. 67–102. DOI: 10.1146/annurev.pc.16.100165.000435.

[7] L. Turner. "Rayleigh-Gans-Born Light Scattering by Ensembles of Randomly Oriented Anisotropic Particles". In: *Appl. Opt.* 12.5 (May 1973), pp. 1085–1090. DOI: 10.1364/AO.12.001085.

[8] S. Cazzato. "Relaxation Dynamics in Amorphous Chalcogenides probed by InfraRed Photon Correlation Spectroscopy". PhD Diss. in Material Science. Università degli Studi di Roma "Sapienza", 2008. URL: https://sites.google.com/uniroma1.it/femtoscopy/theses/discussed-theses/phd (visited on Sept. 11, 2023).

[9] S. N. Yannopoulos. "Athermal Photoelectronic Effects in Non-Crystalline Chalcogenides: Current Status and Beyond". In: *The World Scientific Reference of Amorphous Materials. Amorphous Chalcogenides: Structure, Properties, Modeling and Applications*. Vol. 1. World Scientific, Jan. 2021, pp. 251–319. DOI: 10.1142/9789811215575_0009.

[10] *Datasheet Cobolt 05-01 Series*. HÜBNER Photonics. URL: https://hubner-photonics.com/wp-content/uploads/2014/10/D0350-0_Datasheet-Cobolt-05-01-Series-1.pdf.

[11] F. P. Kent; W. Dudley. "Optical properties of water in the near infrared". In: *Journal of the Optical Society of America* 64.8 (Aug. 1974), pp. 1107–1110. DOI: 10.1364/JOSA.64.001107.

[12] P. R. Cooper. "Refractive-Index measurements of liquids used in conjunction with optical fibers". In: *Appl. Opt.* 22.19 (Oct. 1983), pp. 3070–3072. DOI: 10.1364/AO.22.003070.

[13] M. Born; E. Wolf. *Principles of Optics*. Sixth Edition. Pergamon, 1980. ISBN: 978-0-08-026482-0.

[14] *Datasheet VGA SWIR InGaAs 15µm*. Photonic Science. URL: https://photonicscience.com/wp-content/uploads/2020/05/201905127-Datasheet-VGA-SWIR-InGaAs-15um_Issue2.pdf.

[15] C. Hicks; M. Kalatsky; R. A. Metzler; A. O. Goushcha. "Quantum efficiency of silicon photodiodes in the near-infrared spectral range". In: *Appl. Opt.* 42.22 (Aug. 2003), pp. 4415–4422. DOI: 10.1364/AO.42.004415.

[16] E. Jakeman; E. R. Pike. "The intensity-fluctuation distribution of Gaussian light". In: *Journal of Physics A: General Physics* 1.1 (Jan. 1968), p. 128. DOI: 10.1088/0305-4470/1/1/318.

[17] G. P. Hildred; A. G. Hall. "Intensity fluctuation linewidth and the Jakeman-Pike approximation". In: *Journal of Physics A: Mathematical and General* 11.6 (June 1978), p. L135. DOI: 10.1088/0305-4470/11/6/002.

[18] J. Gabriel; T. Blochowicz; B. Stühn. "Compressed exponential decays in correlation experiments: The influence of temperature gradients and convection". In: *The Journal of Chemical Physics* 142.10 (Mar. 2015), p. 104902. DOI: 10.1063/1.4914092.

[19] *Datasheet BC106N-VIS/M*. Thorlabs. URL: https://www.thorlabs.com/catalogpages/obsolete/2021/BC106N-VIS_M.pdf.

[20] D. Meschede. In: *Optics, Light, and Lasers. The Practical Approach to Modern Aspects of Photonics and Laser Physics*. John Wiley & Sons, Ltd, 2017. ISBN: 9783527685486.

[21] L. Cipelletti; H. Bissig; V. Trappe; P. Ballesta; S. Mazoyer. "Time-resolved correlation: a new tool for studying temporally heterogeneous dynamics". In: 15.1 (Dec. 2002), S257. DOI: 10.1088/0953-8984/15/1/334.

[22] A. Duri; H. Bissig; V. Trappe; L. Cipelletti. "Time-resolved-correlation measurements of temporally heterogeneous dynamics". In: *Phys. Rev. E* 72 (5 Nov. 2005), p. 051401. DOI: 10.1103/PhysRevE.72.051401.

[23] A. Duri; L. Cipelletti. "Length scale dependence of dynamical heterogeneity in a colloidal fractal gel". In: *Europhysics Letters* 76.5 (Nov. 2006), p. 972. DOI: 10.1209/epl/i2006-10357-4.

[24] A. Duri; P. Ballesta; L. Cipelletti; H. Bissing; V. Trappe. "Fluctuations and noise in time-resolved light scattering experiments: measuring temporally heterogeneous dynamics". In: *Fluctuation and Noise Letters* 5.1 (2005), pp. L1–L15. DOI: 10.1142/S0219477505002367.

[25] P. Mayer; H. Bissig; L. Berthier; L. Cipelletti; J. P. Garrahan; P. Sollich; V. Trappe. "Heterogeneous Dynamics of Coarsening Systems". In: *Phys. Rev. Lett.* 93 (11 Sept. 2004), p. 115701. DOI: 10.1103/PhysRevLett.93.115701.

[26] T. L. Alexander; J. E. Harvey; A. R. Weeks. "Average speckle size as a function of intensity threshold level: comparison of experimental measurements with theory". In: *Appl. Opt.* 33.35 (Dec. 1994), pp. 8240–8250. DOI: 10.1364/AO.33.008240.

[27] A.G.M. Ferreira; A.P.V. Egas; I.M.A. Fonseca; A.C. Costa; D.C. Abreu; L.Q. Lobo. "The viscosity of glycerol". In: *The Journal of Chemical Thermodynamics* 113 (2017), pp. 162–182. DOI: https://doi.org/10.1016/j.jct.2017.05.042.

[28] J.B. Segur; H.E. Oberstar. "Viscosity of Glycerol and Its Aqueous Solutions". In: *Industrial & Engineering Chemistry* 43.9 (1951), pp. 2117–2120. DOI: 10.1021/ie50501a040.

[29] M. Giglio; M. Carpineti; A. Vailati. "Space Intensity Correlations in the Near Field of the Scattered Light: A Direct Measurement of the Density Correlation Function $g(r)$". In: *Phys. Rev. Lett.* 85 (7 Aug. 2000), pp. 1416–1419. DOI: 10.1103/PhysRevLett.85.1416.

[30] M. Giglio; M. Carpineti; A. Vailati; D. Brogioli. "Near-field intensity correlations of scattered light". In: *Appl. Opt.* 40.24 (Aug. 2001), pp. 4036–4040. DOI: 10.1364/AO.40.004036.

[31] R. Piazza. "Statistical optics concepts in light scattering and microscopy of colloidal systems". In: *Physics of Complex Colloids:* ed. by C. Bechinger; F. Sciortino; P. Ziherl. International School of Physics "Enrico Fermi". Netherlands, Amsterdam: IOS Press, 2013, pp. 245–315. DOI: 10.3254/978-1-61499-278-3-245.

[32] R. Piazza. *Optical correlation techniques for the investigation of colloidal systems*. Milano, June 2013. DOI: 10.48550/arXiv.1306.1401.